UNIVERSITY OF HELSINKI
FACULTY OF AGRICULTURE AND FORESTRY

Monitoring Scots pine seedlings' response to drought using hyperspectral imaging

Iiro Miettinen

Master's Thesis

University of Helsinki
Master's Program of Forest Sciences
Forest Ecology and Management

May 2023

Tiedekunta/Osasto Fakultet/Sektion – Faculty	Laitos/Institution– Department
Faculty of Agriculture and Forestry	Department of Forest Sciences

Tekijä/Författare – Author

Iiro Miettinen

Työn nimi / Arbetets titel – Title

Monitoring Scots pine seedlings' response to drought using hyperspectral imaging

Oppiaine /Läroämne – Subject

Forest Ecology and Management

Työn laji/Arbetets art – Level	Aika/Datum – Month and year	Sivumäärä/ Sidoantal – Number of pages
Master's Thesis	May 2023	44 + appendices

Tiivistelmä/Referat – Abstract

Forests' exposure to drought is increasing as a result of climate change. Drought increases tree mortality and the likelihood of wildfires. Mitigating damages contributed to by drought is important in order to secure access to ecosystem services. Remote sensing can be applied in drought detection, development monitoring, wildfire risk assessment, and phenotyping for resistance breeding. Hyperspectral imaging (HSI) combines spectral and spatial information, which may be used as a proxy to estimate biochemical and physiological traits of plants, including water content and response to water stress. More affordable and compact HSI cameras have become available in recent years, but their use in remote sensing of forests is still somewhat novel. The photochemical reflectance index (PRI) is an optical vegetation index, that was originally defined based on its diurnal response to the epoxidation state of xanthophyll cycle. PRI has been successfully used to capture drought stress and recovery on various scales on mainly broadleaf species. PRI responds to drought due to stomatal closure leading to downregulation of photosynthesis increasing the need for light energy dissipation. The aim of this thesis was to assess the feasibility of monitoring drought development and recovery of *Pinus sylvestris* seedlings in ambient greenhouse conditions using hyperspectral imaging. The hypotheses addressed in this thesis were: 1) there is a relationship between physiological variables and optical vegetation indices from HSI, and 2) PRI captures reversible photoprotective energy dissipation and responds to stress, outperforming the chlorophyll-responsive indices over the duration of the drought and recovery period. Imaging and additional measurements were performed on 8 4-year-old *Pinus sylvestris* seedlings. *Pinus sylvestris,* is the most common tree species in Finland, and it is widely utilized in the Finnish forestry industry. Half of the seedlings were exposed to 17 days of progressive drought and half were watered regularly. HSI and physiological variables were measured every few days for the duration of pre-drought, drought, and recovery periods. Physiological variables, which were leaf water potential and maximum quantum yield of PSII photochemistry (F_v/F_m), were measured to validate drought stress development. Additionally, meteorological conditions and soil moisture content were monitored. Non-imaging leaf level reflectance was measured on 3 days, which represented pre-drought, height of drought, and end of recovery. This thesis is concerned with the data collected on these three days. The results of this thesis showed that HSI based PRI between drought and control plants differentiated significantly during height of drought, and mostly recovered by the end of the scheduled recovery period. Chlorophyll-responsive red edge index responded to drought but did not show signs of recovery. Relationship between HSI based PRI and physiological variables F_v/F_m and leaf water potential was significant. These results demonstrate that HSI can be used to capture progressive drought stress development and recovery at a seedling canopy level in boreal evergreen saplings under greenhouse conditions.

Avainsanat – Nyckelord – Keywords

Scots pine, hyperspectral imaging, drought stress, xanthophyll cycle, photochemical reflectance index, PRI, red edge, REP, leaf water potential, *Fv/Fm*

Säilytyspaikka – Förvaringställe – Where deposited

Helsinki University Library – Helda / E-thesis (opinnäytteet) ethesis.helsinki.fi

Muita tietoja – Övriga uppgifter – Additional information

Tiedekunta/Osasto Fakultet/Sektion – Faculty	Laitos/Institution– Department
Maatalous-Metsätieteellinen tiedekunta	Metsätieteiden osasto

Tekijä/Författare – Author

Iiro Miettinen

Työn nimi / Arbetets titel – Title

Männyntaimien kuivuusstressin seuranta hyperspektraalikuvantamisella

Oppiaine /Läroämne – Subject

Metsien ekologia ja hoito

Työn laji/Arbetets art – Level	Aika/Datum – Month and year	Sivumäärä/ Sidoantal – Number of pages
Maisterin tutkielma	Toukokuu 2023	44 + liitteet

Tiivistelmä/Referat – Abstract

Metsien altistuminen kuivuudelle yleistyy ilmastonmuutoksen johdosta. Kuivuus lisää puiden kuolleisuutta, ja kasvattaa metsäpalojen riskiä. Kuivuuden aiheuttamien vahinkojen lieventäminen on tärkeää, jotta metsien tarjoamien ekosysteemipalveluiden saatavuus olisi turvattu. Kaukokartoitusmenetelmiä voidaan soveltaa kuivuuden havaitsemiseen ja seuraamiseen, metsäpaloriskin arviointiin ja fenotyypin arviointiin resistenssijalostusta varten. Hyperspektrikuvantaminen (HSI) on spektrisen ja spatiaalisen informaation yhdistelmä, jota voidaan hyödyntää kasvien biokemiallisten ja fysiologisten ominaisuuksien, mukaan lukien vesipitoisuuden, epäsuorassa arvioinnissa. Viime aikoina markkinoille on saapunut edullisia ja pienikokoisia HSI-kameroita, joiden käyttö on ollut metsien ja puiden kaukokartoituksessa toistaiseksi vähäistä. *Photochemical reflectance index* (PRI) on optinen kasvillisuusindeksi, joka perustuu ksantofyllisyklin epoksidaatio-asteeseen. PRI:tä on onnistuneesti käytetty kuivuusstressin kehityksen ja elpymisen monitoroinnissa lähinnä lehtipuilla. Kuivuuden vaikutus PRI:n perustuu kasvin suurempaan tarpeeseen valoenergian dissipaatiolle. Tämä johtuu siitä, että kasvi sulkee lehtiensä ilmaraot välttääkseen nesteen haihtumisen ja ohessa rajoittaa hiilidioksidin saatavuutta ja sitä kautta fotosynteesiä. Tämän tutkielman tavoite oli arvioida *Pinus sylvestris* taimien kuivuuden kehityksen ja elpymisen seurantaa HSI-kameran avulla kasvihuoneolosuhteissa. Tutkielman hypoteesit ovat: 1) fysiologisten muuttujien ja optisten HSI:n perustuvien kasvillisuusindeksien välillä on suhde, ja 2) kasvia valolta suojaava energian dissipaatio sekä stressireaktio voidaan havaita PRI:n avulla, ja se kuvaa niitä paremmin kuin klorofylliin pohjautuvat indeksit kuivuus- ja elpymisjakson aikana. Kuvantaminen ja oheismittaukset toteutettiin 8:lle 4-vuotiaalle *Pinus sylvestris* taimelle. *Pinus sylvestris* eli metsämänty on Suomen yleisin puu ja hyvin merkittävä suomalaiselle metsätaloudelle. Puolet taimista altistettiin 17 päivän kuivuusjaksolle ja loppuja kasteltiin säännöllisesti. Mittaukset ja HSI kuvantaminen toteutettiin muutaman päivän välein ennen kuivuusjaksoa, sen aikana ja elpymisjaksossa. Mitattavia fysiologisia muuttujia olivat lehtien vesipotentiaali ja PSII-valokemian maksimaalinen kvanttisaanto (F_v/F_m). Lisäksi meteorologisia olosuhteita ja maan suhteellista kosteutta seurattiin. Lehtitason heijastavuus mitattiin kuidulla ennen kuivuusjaksoa, sen huipulla ja elpymisjakson päätteeksi. Tämän tutkielma tarkasteli lähinnä dataa, joka kerättiin näinä kolmena päivänä. Tulokset osoittivat, että HSI:n pohjautuva PRI havaitsi kuivuusstressin kehityksen ja siitä palautumisen. Klorofylliin pohjautua REP-indeksi laski kuivuuskäsittelyn myötä, mutta ei osoittanut elpymisen merkkejä. HSI PRI:n ja fysiologisten muuttujien suhde oli myös merkittävä. Nämä tulokset osoittavat, että HSI:tä voidaan soveltaa kasvihuoneolosuhteissa kokonaisten boreaalisten ikivihreiden puuntaimien progressiivisen kuivuuden kehityksen ja elpymisen seurannassa.

Avainsanat – Nyckelord – Keywords

mänty, hyperspektraalikuvantaminen, kuivuusstressi, photochemical reflectance index, PRI, red edge, REP, lehden vesipotentiaali, *Fv/Fm*

Säilytyspaikka – Förvaringställe – Where deposited

Helsinki University Library – Helda / E-thesis (opinnäytteet) ethesis.helsinki.fi

Muita tietoja – Övriga uppgifter – Additional information

PREFACE

I would like to thank my supervisors Dr. Chao Zhang, Dr. Jon Atherton, and Dr. Luis Alonso-Chorda in helping me complete this thesis.

This master's thesis has received faculty (Faculty of Agriculture and Forestry, University of Helsinki) funding (7800413) as a part of supervisor Dr. Chao Zhang's (Optics of Photosynthesis Lab, University of Helsinki, Finland) Postdoctoral research fellowship from Academy of Finland project SensBVOCs (1340744).

Contents

ABBREVIATIONS

EPS – Epoxidation states

FWHM – Full Width at Half Maximum

GFS – Gas -exchange and Fluorescence System

HSI – Hyperspectral Imaging

LWP – Leaf Water Potential

NIR – Near infra-red spectrum (750-1000 nm)

NPQ – Non-photochemical Quenching

PAM – Pulse-amplitude Modulation fluorescence

PAR – Photosynthetically Active Radiation

PPFD – Photosynthetic Photon Flux Density

PRI – Photochemical Reflectance Index

REP – Red Edge Position

SWIR – Shortwave infra-red spectrum (1000-2500 nm)

VI – optical Vegetation Index

1 INTRODUCTION

Drought severity and frequency is increasing due to climate change (IPCC, 2019). This has serious implications on the health of forests, and as an extent, the availability of ecosystem services dependent on forests. Experiencing water stress leads to physiological changes in trees leading to impaired growth and increased mortality (Mitchell et al., 2013; Semerci et al., 2017). For example, the photosynthetic efficiency of trees declines as stomata close in order for the plant to limit water loss due to transpiration, which limits the intake of CO_2 through stomata (Tyree, 2003). Eventually, prolonged drought will lead to death caused by either hydraulic failure or depletion of available carbohydrate storages (Mitchell et al., 2013). Besides increased mortality and loss of forest ecosystem services, low fuel moisture content, which is defined as the ratio of water mass to total plant dry mass, is associated with an increased risk of wildfires (Chuvieco et al., 2020).

Remote sensing based approaches to drought detection and drought response monitoring could aid in mitigating direct and indirect losses caused by drought (Chuvieco et al., 2020; Ensminger, 2020). Remote sensing technologies allow for the collection of spatial information and scaling across space. Additionally, as remote sensing is non-destructive, repeat measurements can be performed on the same sample and development of drought symptoms can be followed temporally (D'Odorico et al., 2021). Hyperspectral imaging (HSI) is a remote sensing approach that integrates spatial and spectral information (Mishra et al., 2020; Sarić et al., 2022). Previous research has demonstrated that spectral information alone can provide diagnostic tools for detecting water content in plants (Imanishi et al., 2004; Zhang et al., 2017). HSI could add a spatial dimension to spectral drought monitoring, and aid for example in phenotyping for resistance breeding purposes. There is currently a technological gap between existing phenotyping platforms and genotyping methodologies, which HSI could potentially bridge (Feng et al., 2020). While HSI has already been utilized in satellite and aerial imaging since the 1960s, its use has been limited due to high costs and inaccessibility. Recently, compact, and more affordable HSI cameras have entered the market. These systems have been applied in various fields including agriculture, medicine, and food technology (Khan et al., 2018). Nevertheless, their use in remote sensing of properties of trees and forests remains somewhat novel.

I first review the necessary scientific and theoretical background and then form the hypotheses for the thesis.

1.2 Theoretical background

1.2.1 Spectroscopy in plant science

Spectroscopy refers to the measurement of the interaction between an object, such as a plant, and electromagnetic radiation (Roy, 1989). When electromagnetic radiation interacts with a plant, radiation is either transmitted, absorbed, or reflected (Roy, 1989; Zahir et al., 2022). Additionally, a small amount of electromagnetic radiation is re-emitted after absorption by the plant's pigments as fluorescence. Fluorescence consist of photons in the red spectral range re-emitted by chlorophyll in photosystem II (PSII) returning to a lower excitation state instead of the absorbed energy being utilized in photochemistry (Porcar-Castell et al., 2014). Plant spectroscopy is often concerned with reflectance in the visible and near infra-red regions of electromagnetic radiation (Roy, 1989; Zahir et al., 2022). In this context, spectral reflectance refers to the portion of radiation reflected by a surface from total radiation received by that surface, and is thus either denoted as a value between 0 and 1 or a percentage at a given wavelength (Roy, 1989).

In plant science, spectral data can be used as a proxy for various physiological and biochemical properties and functions of plants (Zeng et al., 2022). For example, liquid water has distinct absorption peaks in NIR and shortwave infra-red (SWIR) domains, which in a plant's spectral signal translate to absorption features caused by leaf water in the same regions (Watt et al., 2021). In a reflectance curve, these high absorption features appear as low reflectance. Spectroscopy has also been applied in determining protein-bound nitrogen content in dried plant matter by using absorption features in NIR and SWIR domains caused by N-H bond stretching (Féret et al., 2021). SWIR spectroscopy can also be used to assess phosphorous and hemicellulose content (Sarić et al., 2022).

Radiation in the visible electromagnetic spectrum (400-750 nm) has been extensively utilized in photosynthetic research, because plant pigments involved in photosynthesis have strong absorption features in this region (Wong et al., 2020; Zeng et al., 2022). Vital to photosynthesis, the two types of chlorophyll in green plants, chlorophyll a and b, have maximum absorption in the blue and red ranges of visible light. Due to chlorophyll absorbance, reflectance in the green spectrum is higher in relation to the blue and red regions, which is why plants appear green overall (Carvalho et al., 2011). Other pigment families have differing absorption patterns. For example, anthocyanins have maximum absorbance in the green region (530-550 nm), and carotenoids in the blue to green region (Carvalho et al., 2011). Consequently, changes in the concentrations of pigments can cause changes to the plant's spectral properties, which can be detected with visible spectroscopy (Zahir et al., 2022). Changes in these pigments can act as a proxy for photosynthesis, so as an extension, using certain bands in the visible region and spectroscopic methods, variation in photosynthetic activity can be monitored (Zeng et al., 2022).

1.2.2 Optical vegetation indices

Features in a plant spectral curve are often actualized by calculating optical vegetation indices (VIs). These VIs are calculated using two or more specific spectral bands (Sarić et al., 2022). For example, the normalized difference vegetation index (NDVI) is a common VI used as an indicator of green vegetation in aerial imaging and is calculated as the red: NIR reflectance ratio. NDVI is based on the low reflectance of plants in the red region due to chlorophyll absorbance, and high scattering in the NIR region (Pettorelli et al., 2005). Although NDVI is partially based on chlorophyll absorbances, it cannot be used as a reliably proxy for chlorophyll content, as the scattering in NIR is greatly affected by other factors including brightness of the canopy and soil (Xue and Su, 2017).

The photochemical reflectance index (PRI) is another widely used VI. It was originally defined based on its sensitivity to the epoxidation state (EPS) of the xanthophyll cycle (Gamon et al., 1992, 1990). The xanthophyll cycle refers to the reversible enzymatic de-epoxidation of the pigment violaxanthin into antheraxanthin and further into zeaxanthin

(Fig. 1). This de-epoxidation happens under excessive light conditions and is reversed in limiting light (Yamamoto and Kamite, 1972; Yamamoto, 1979). The xanthophyll cycle is an essential part of photoprotective non-photochemical quenching (NPQ), which is a mechanism through which a plant dissipates excessive absorbed light energy and evades damage to PSII caused by photooxidation (Gamon et al., 1990, 1992; Wong et al., 2020). EPS correlates with reflectance at around 531 nm (R_{531}), which is why PRI is calculated using R_{531} and a reference band R_{570} at 570 nm (Gamon et al., 1990),.

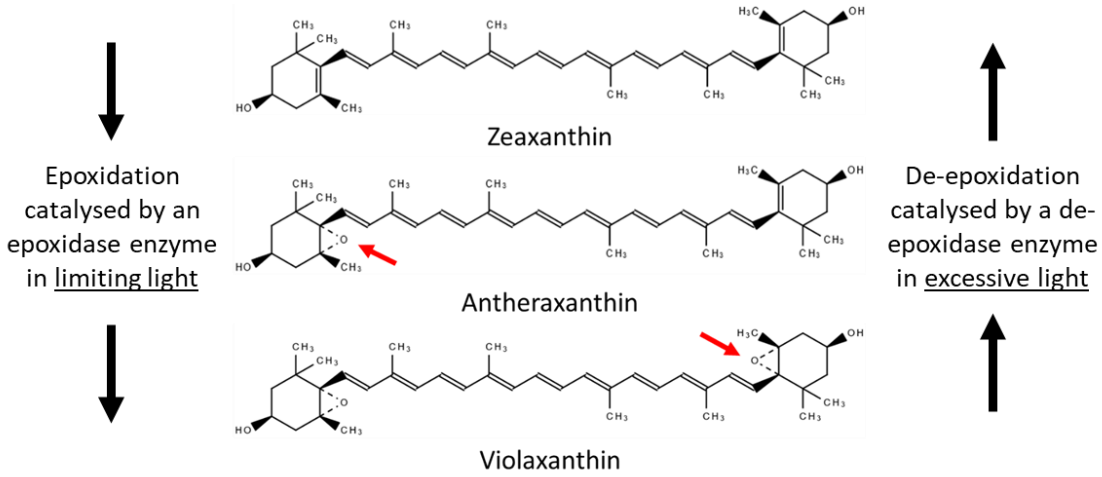

Figure 1. The xanthophyll cycle or the de-epoxidation of violaxanthin into zeaxanthin via antheraxanthin. The red arrow points to the epoxide groups either enzymatically lost or gained depending on the light conditions in each transformation. This figure is modified from Fig. 1 in Gamon et al., (1992) and Fig 2. in Demmig-Adams, (1990).

Undergoing drought stress leads to downregulation of photosynthesis. This is contributed to by the closing of stomatal openings. Stomata closes in order to preserve water and avoid water loss by transpiration. This leads to lower intake of CO_2, which is vital to photosynthesis. Consequently, this downregulation causes the level on which photosynthesis is saturated and light conditions are excessive to be lower. This increases the need for energy dissipation via the xanthophyll cycle in order to prevent photooxidation (Demmig-Adams and Adams, 1996; D'Odorico et al., 2021). As a result, PRI should be able to capture drought stress by detecting increased reversible photoprotective energy dissipation in comparison to a non-drought stressed control. The function of PRI as an indicator of drought has been demonstrated on various scales using different species of mainly broadleaf trees. Suárez et al. (2008) reported that on a canopy

level, the PRI of olive orchard trees was sensitive to drought, but also affected by diurnal dynamics. Ripullone et al. (2011) reported a 30-50% decreased in leaf level PRI in water stressed trees of different broadleaf species with the exception of *Populus euroamericana*. As there is apparent interspecies variability, it is notable that PRI response to drought has also been reported in conifers. D'Odorico et al. (2021) successfully monitored the drought affected PRI of mature Scots pines using drone-based multispectral imaging.

Besides capturing short-term diurnal and stress induced cycles in EPS, PRI also captures long-term seasonal down-regulation of boreal evergreen conifers (Wong et al., 2020; Wong and Gamon, 2015; Yang et al., 2020). But as the xanthophyll cycle becomes inactive during colder seasons, this seasonal change correlates with overall chlorophyll: carotenoid ratio rather than changes in EPS (Gamon et al., 2015; Wong and Gamon, 2015). It is thus likely that the slower build-up of other carotenoids, like lutein, contribute to photoprotection during this season (Wong and Gamon, 2015). During spring recovery, the xanthophyll cycle reactivates in the early spring, indicating the activation of PSII. This is followed by changes in pigment pool ratios characterized by increased chlorophyll and decreased carotenoids in relation to chlorophyll. Thus, the seasonal PRI cycle is governed by this shift (Gamon et al., 2015; Wong and Gamon, 2015).

The red edge position (REP) refers to a point of local maximum slope located in the red to near-infrared region between 680 and 750 nm (Cho and Skidmore, 2006; Filella and Penuelas, 1994). This region coincides with the long wavelength end of the chlorophyll absorption feature, where the plants reflectance curve shifts steeply from low reflectance, due to the strong absorbance by chlorophyll in the red spectral region, to high reflectance in the NIR region due to high scattering. Because of higher chlorophyll content shifts REP towards longer wavelengths, REP can be used as an indicator of chlorophyll content. Red edge parameters like REP are also affected by water stress, as water absorbance affects reflectance in the immediate NIR region (Filella and Penuelas, 1994).

1.2.3 Hyperspectral imaging

Hyperspectral imaging (HSI) captures spatial information simultaneously with corresponding spectroscopic information from tens to thousands of wavelengths. The output of HSI is a cube consisting of two spatial dimensions (x and y), and one spectral dimension consisting of the pre-selected wavelength bands (Mishra et al., 2020; Sowmya et al., 2019). Each pixel, in addition to a two-dimensional coordinate location, has radiance values corresponding to all the spectral bands of the cube's spectral dimension. Fig. 2 illustrates the three dimensions of an HSI cube, and a reflectance curve corresponding to one plant pixel. Reflectance curves of a single pixel or a masked area can be used to calculate VIs.

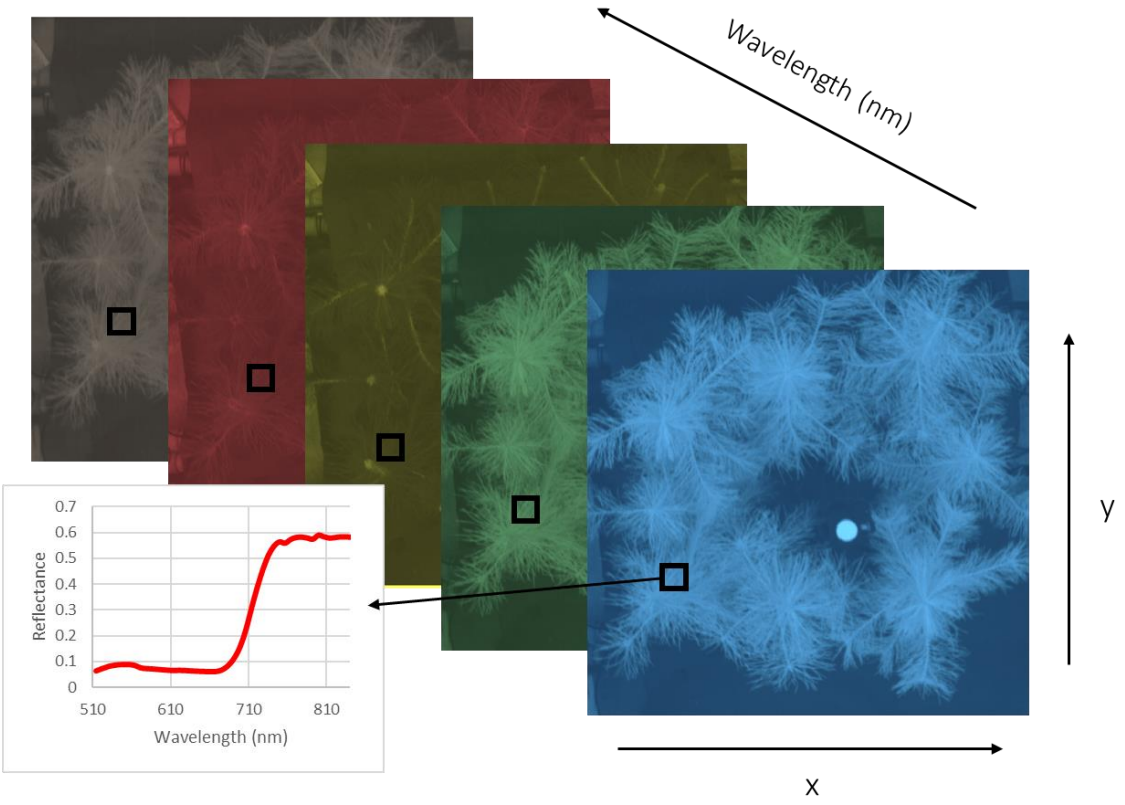

Figure 2. A diagram illustrating the spatial x- and y-dimensions, and the spectral dimension of a hyperspectral cube and a reflectance curve corresponding to one pixel.

HSI cameras have different data capturing approaches. These include point-scanning, line-scanning, and snapshot imaging (Sarić et al., 2022). Point-scanning, also called

whiskbroom scanning, involves the scanning of the whole spectral dimension at once, but spatially pixel by pixel. Line-scanning cameras also measure the whole spectral dimension instantly but proceed in pixel rows. Snapshot cameras scan the full spatial area simultaneously. They can proceed on the spatial dimension one wavelength band at a time or scan multiple bands simultaneously.

1.3 Hypothesis and detailed aims

This thesis aims to assess the feasibility of hyperspectral imaging in capturing progressive drought stress development and recovery at a shoot level in boreal evergreen saplings under greenhouse conditions. The two hypotheses addressed in this thesis are as follows: 1) there is a relationship between physiological variables (chlorophyll fluorescence parameter F_v/F_m and leaf water potential) and optical vegetation indices from hyperspectral imaging, and 2) the photochemical reflectance index captures reversible photoprotective energy dissipation and responds to water stress, outperforming the chlorophyll-based indices during the drought and recovery period.

2 MATERIAL AND METHODS

2.1 Research material

The material of this thesis consists of hyperspectral images, and physiological and supporting data based on measurements performed on 8 individual 3-year-old *Pinus sylvestris* seedlings (Fig. A1 in Appendix 1) in August and September 2022. Sampling and imaging was focused on current year needles in the primary shoot, which had reached maturity by the start of the experiment. For the duration of the experiment, the seedlings were grown in individual pots inside a greenhouse room in ambient conditions. Before the start of the experiment, the seedlings were brought to the greenhouse in mid-May and had thus adapted to greenhouse conditions. During treatment, half of the seedlings were exposed to 18 days of drought, and half acted as control and were watered regularly. Treatment assignment and position within the imaging grid was determined at random.

Measurements and imaging were concentrated around three primary measurement days, which were: pre-drought (Aug 9th), height of drought (Aug 31st), and end of recovery (Sep 8th). Non-imaging-based leaf level reflectance was only measured on these three days using an OceanOptics USB2000+ (Ocean Optics®, Largo, FL, USA) spectrometer under a white LED at photosynthetic photon flux density (PPFD) of 1000 $\mu mol \cdot m^{-2} \cdot s^{-1}$. Physiological and supporting traits, which consisted of the maximum quantum yield of PSII photochemistry of dark accumulated leaves (F_v/F_m), leaf water potential (LWP, Bar), and relative soil moisture (SM, %), were measured every few days for the duration of pre-drought, drought, and recovery periods. The detailed measurement schedule is available in Table A1 in Appendix 2.

2.1.1 Meteorological and soil conditions

Temperature within the greenhouse was logged at a 5-minute interval, and outside PPFD ($\mu mol \cdot m^{-2} \cdot s^{-1}$) every 1 hour, by pre-existing meteorological infrastructure. PPFD within the greenhouse was recorded manually during the HSI protocol once per image. Relative soil moisture (%) was measured at a depth of 10 cm in the random selected locations using an ML3 ThetaProbe soil moisture sensor with an HH2 Soil Moisture Meter (Delta-T Devices Ltd., Cambridge, UK). Due to the heterogeneity of the potting soil, measurements were taken thrice per pot per day and averaged.

2.1.2 Leaf-water potential

Leaf water potential (LWP), which is representative of a leaf's ability to retain water, was measured daily or every 2 to 3 days for the duration of the experiment using a pressure chamber (Model 1505D-EXP, PMS Instrument Company). Besides adjustments related to accommodating conifer needles, LWP was measured following the method described by Scholander et al. (1965).

A pair of needles from the top of the primary shoot was used for each individual measurement, and 2 to 4 repeats were performed for each seedling per day of measurement. Needles were extracted between 9:00 and 10:00 and measured immediately.

The base of harvested needles was cut with a surgical knife before fitting them in an air-tight pressure chamber. The exposed surface outside the mouth of the pressure chamber was observed with the aid of a magnifying glass and a light, while pressure was gradually increased within the system. The pressure at which the exposed base of the needle turned wet was noted. This value is equal and opposite to the value of LWP.

2.1.4 Non-imaging-based leaf level reflectance

Leaf spectral reflectance was obtained by using a UV-VIS spectrometer OceanOptics® USB 2000+ (Ocean Optics®, Largo, FL, USA) under a white LED light (LED 3041-L, Walz, Heinz Walz GmbH, Effeltrich, Germany) at PPFD 1000. The fiber optic of the spectrometer had been fitted into the leaf chamber of a gas-exchange and fluorescence system (GFS3000, Heinz Walz GmbH, Effeltrich, Germany) measuring head (Fig. A3 in Appendix 3). The measurement was conducted at a c. 60° angle and c. 2 mm distance, with integration time of 40 ms on Aug 9th, and 25 ms on Aug 31st and Sep 8th. White reference and dark current spectra were collected before the reflected radiation spectra, with 20 to 30 spectra for each measurement.

2.1.5 Hyperspectral imaging

HSI measurements were performed using a snapshot Senop HSC-2 Hyperspectral camera (Senop Ltd., Helsinki, Finland) with a 510-900 nm wavelength range, which corresponds to the visible and partial NIR region. Images were taken at the top of the canopy of all 8 seedlings from a distance of 97 to 108 cm and an off-nadir angle of 8.4 to 19.7°. The exact distance and angle to each plant shoot from the lens is available in Table A2 in Appendix 4.

The extent of the spatial dimensions of the HSI data cubes were 1024 * 1024 pixels, whilst the spectral dimension consisted of 52 bands. The spectral bands selected for the protocol were centred at 50 evenly distributed wavelengths between 500 and 850 nm. Additionally, bands centred at 531 nm and 570 nm were included for PRI calculation. The camera is capable of operating at three different bandwidths (‘wide’, ‘normal’, and ‘narrow’).

Narrow bandwidth was selected for all measurements. The exact wavelength positions of band centres, and their corresponding bandwidths are available in Table A3 in Appendix 5.

Each HSI measurement resulted in 8 data cubes, 4 of which were sample images with different integration times (exposures), and 4 were dark currents with corresponding integration times. Dark currents were taken with the camera's lens cap on, and they are representative of the minimum signal and relate to overall noise (Paulus and Mahlein, 2020). The HSI camera has two detectors, which operate on different spectral ranges, but have an overlap around 640 nm. Due to differences in the sensors' sensitivity, integration times were manually optimized for both separately. In short, the integration times for the 4 sample cubes were optimized for: 1) seedlings at 531 nm (sensor 1), 2) white reference at 531 nm (sensor 1), 3) seedlings at 800 nm (sensor 2), and 4) white reference at 800 nm (sensor 2). The white reference was a white flat panel made from material with an assumed 100% reflectivity, which was placed on a tripod at the median height of the seedling canopy. PPFD measured with a photosynthetically active radiation (PAR) sensor, and a real-time histogram of pixel values provided within the Senop HSI-2 Software (Senop Ltd., Helsinki, Finland), were used as aid in optimizing the integration time. The imaging protocol of 8 cubes was repeated 3 to 4 times consecutively on each day of measurement. The imaging script was devised and executed using Senop HSI-2 Software.

2.1.3 Pulse-amplitude modulation chlorophyll fluorescence

Chlorophyll fluorescence parameters can be used to estimate the amount of light energy used in photochemistry, or alternatively, dissipated as heat and fluorescence. In this thesis, the maximum quantum yield of PSII photochemistry (F_v/F_m) was estimated using pulse-amplitude modulation (PAM) as first developed by Schreiber et al. (1986). The instrument used was the Chlorophyll Fluorometer PAM-2500 (Heinz Walz GmbH, Effeltrich, Germany). The F_v/F_m-ratio was calculated automatically by the instrument as described in Genty et al. (1989):

$$\frac{F_v}{F_m} = \frac{F_m - F_0}{F_m}$$

in which F_0 is minimal fluorescence, and F_m is maximal fluorescence.

Minimal fluorescence (F_0) was gained by measuring the fluorescence level of a dark-adapted leaf using the measuring light, and maximum fluorescence (F_m) was gained by measuring the fluorescence level of the dark-adapted leaf under a saturating light pulse. F_0 and F_m were measured in succession by the instrument.

PAM measurements were performed in the morning on dark accumulated current year needles of the primary shoot. Dark-adaptation clips were placed on the sampled needles at least 20 minutes before measurement as seen in Fig. A2 in Appendix 3. Three repeats per tree for each day of measurement were carried out, and an average of the repeats was used in analysis.

2.2 Data Analysis

2.2.1 Processing of supporting data

All manually collected non-imaging-based data (relative soil moisture, LWP, F_v/F_m, and indoor PPFD during HSI) was compiled into a CSV-file and processed in R Statistical Software (v4.2, R Core Team 2023). Additionally, indoor temperature and outdoor PPFD were retrieved from pre-existing climate logging infrastructure.

Pre-processing of non-imaging-based leaf level reflected radiation was done by supervisor Dr. Chao Zhang (Optics of Photosynthesis Lab, University of Helsinki, Finland). This included manual selection of data and calculation of average raw signal for samples, dark currents, and white references. Post-processing was done in R Statistical Software (v4.2, R Core Team 2023), and consisted of calculation of reflectance, visualization of data, and calculation of VIs. Additionally, spectral signals of samples collected on pre-drought (Aug 9th) were transformed by the difference in signal at 420 nm between plant 6C. Reflectance was calculated as:

$$R = \frac{S_{DN} - DC_{DN}}{WR_{DN} - DC_{DN}}$$

in which S_{DN} is the raw reflected radiation of sample in digital numbers (DN), DC_{DN} is the dark current in DN, and WR_{DN} is the raw reflected radiation of the white panel in DN.

2.2.2 HSI processing

2.2.2.1 Pre-processing

In this thesis, HSI pre-processing refers to all steps concerned with processing a raw data cube consisting of DN to a reflectance cube. Pre-processing steps were done by Dr. Luis Alonso Chorda (Optics of Photosynthesis Lab, University of Helsinki, Finland) using the IDL® scripting language (v8.8.3).

Before reflectance calculations, images were normalized by integration time, and images with excessive saturation were excluded. Pre-processing also addressed problems with the camera itself, including issues related to the system relying on two separate sensors. As a results of the separate sensors, cubes had different noise levels and spatial pattern in the visible and NIR ranges. Overall, the bands located at the overlap of the sensors and at the terminal wavelengths were extremely noisy and were exluded. A spatial offset of approximately 9 x 2 pixels between the sensors was also detected. Accurate realignment of layers was crucial, as needles may already be sub-pixel targets, and an offset of several pixels will completely displace the target between bands imaged by different sensors (L. Alonso Chorda, personal communication, Feb 2023).

After normalization, selection of data, spatial realignment, and noise reduction steps, a hyperspectral cube consisting of reflectance, $cube_R$, was calculated as:

$$cube_R = \frac{cube_{raw} - cube_{DC}}{WR - cube_{DC}}$$

in which $cube_{raw}$ is the raw output of the camera consisting of DN, $cube_{DC}$ is the dark current cube, and WR is the white reference value derived from the white reference panel included in the raw image.

2.2.2.2 Post-processing

In this thesis post-processing refers to all processing steps performed on a reflectance cube. These steps are as follows: 1) masking individual shoots, 2) calculation of VIs, 3) data visualization, and 4) statistical analysis. Post-processing was done using R Statistical Software (v4.2; R Core Team 2023), and all packages used, and functions written, are available in Appendix 6.

The aim of masking the HSI images was to extract individual shoots and to remove gaps between needles. This was done by filtering pixels with NDVI values lower than 0.7, and by applying a circle mask with a radius of 80 pixels and a focus that was manually estimated to be at the center of the primary shoot. An example of a masked shoot in comparison to a RGB image can be seen in Image 6 below.

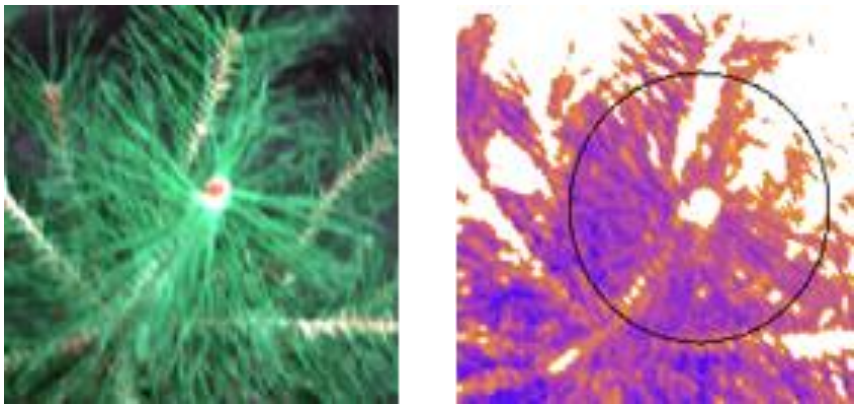

Figure 3. A RGB close-up of the shoot of plant 10D (left) and NDVI (right). Pixels in which NDVI < 0.7 have been removed and are depicted white. The black circle denotes the limits of the circle mask.

VIs were calculated in R Statistical Software (v4.2; R Core Team 2023) by performing operations on two-dimensional raster layers corresponding to spectral dimensions at set

wavelength bands. The output was a two-dimensional raster of VI values, in which one value corresponded to one pixel in the image. These layers were graphed as images for visualization purposes. Mean of VI values was calculated for each masked area, so that the final output was one VI value descriptive of one plant.

NDVI was calculated for filtering purposes in this thesis as:

$$NDVI = \frac{R_{NIR} - R_{RED}}{R_{NIR} + R_{RED}}$$

in which R_{NIR} is reflectance at the band centered at 850 nm, and R_{RED} is average reflectance on bandwidths centered at 620 to 640 nm. The width of the signal at 50% of its maximum intensity (FWHM) of the RED-bands was 13-16 nm, and 17 nm of the NIR-band.

On all days except pre-drought (Aug 9th), PRI was calculated using the exact bands as defined by Gamon et al. (1992). The formula for PRI used in this thesis was:

$$PRI = \frac{R_{531} - R_{570}}{R_{531} + R_{570}}$$

in which R_{531} is reflectance of a band centered at 531 nm, and R_{570} reflectance of a band centered at 570 nm. The FWHM bandwidths of bands 531 and 570 nm were 13 and 12 nm respectively. On pre-drought R_{570} was reflectance of a band centered at 571.4 nm, as a band at 570 nm was not available.

REP (nm) was determined by linear four-point interpolation as suggested by Guyot and Baret (1988):

$$REP(nm) = 700 + 40\ \frac{R_i - R_{700}}{R_{740} - R_{700}}$$

in which R_{700} and R_{740} are reflectance at 700 and 740 nm, and R_i is reflectance at inflection point *i*, which is defined as:

$$R_i = \frac{R_{670}+R_{780}}{2}$$

in which R_{670} is reflectance at 670 nm and R_{780} reflectance at 780 nm (Cho and Skidmore, 2006).

In this thesis band centered at the exact wavelength suggested by Gyot and Baret (1988) were not available, so the nearest equivalent bands in the HSI cube were used. These were 700, 742.9, 671.4 and 778.6 nm, and their FWMH bandwidths were 14, 14, 14, and 13 nm respectively. The location of the bands used to calculate PRI and REP in this thesis are demonstrated in Fig. 4 with a reference plant reflectance curve.

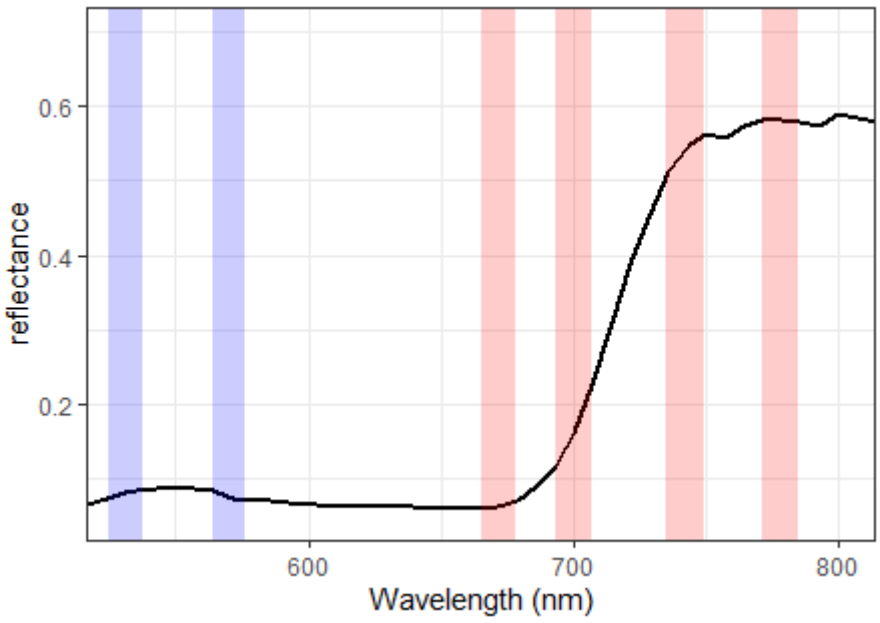

Figure 4. The black solid line denotes a plant's (plant 9D on Aug 9th) reflectance in the spectral range of the HSI camera. The bands used to obtain PRI are demonstrated by the blue shaded areas and REP by the red shaded areas. The width of the shaded area corresponds to the bands' FWMH bandwidth.

2.2.3 Statistical analysis

Statistical analysis was done using R Statistical Software (v4.2; R Core Team 2023). Timeseries of meteorological and supporting variable (LWP and F_v/F_m) development were generated to assess the development of physiological drought and surrounding

conditions. The difference between value distribution of physiological variables between treatment groups within each measuring day was tested using the Wilcoxon rank-sum test. Additionally, correlations between all measured variables, including VIs, were assessed by calculating Pearson's r (ρ) and compiling them into a correlation matrix. The relationship of PRI based on HSI and leaf level reflectance and supporting variables (LWP and F_v/F_m) was assessed by applying linear regression and by calculating the coefficient of determination, R^2.

3 RESULTS

3.1 Supporting and physiological variables

Temperature within the greenhouse varied drastically during the 31 days sampling took place over, with 9 of the warmest days reaching over 30 °C, while the coolest remained sub 20 °C. In total, 18 days temperature climbed above 25 °C. Similarly, outdoor PPFD also changed drastically between days, being over two-fold on the brightest days in comparison to the most overcast days. The variation of indoor temperature and outdoor PPFD is depicted in a timeseries in Fig. 5.

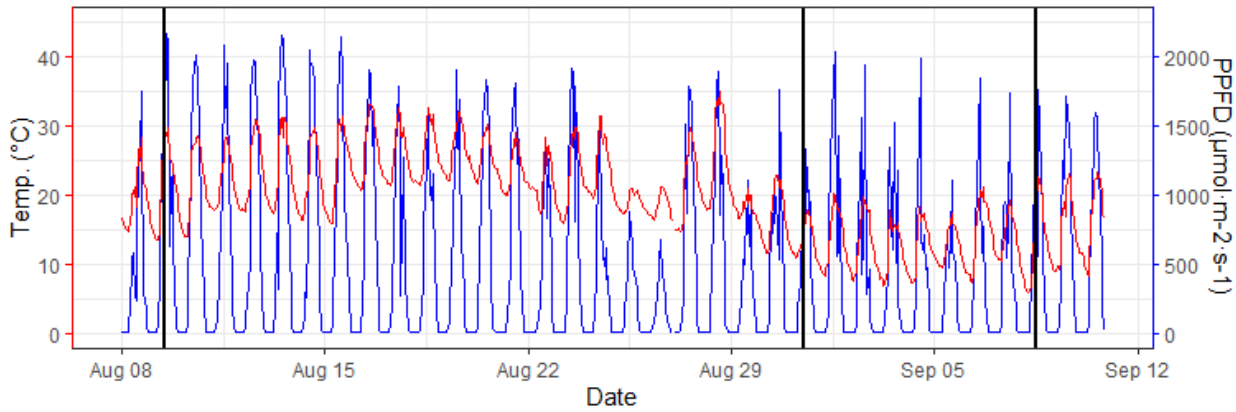

Figure 5. Timeseries of greenhouse room temperature in °C (red) and outdoor PPFD (blue). The black vertical lines denote the pre-drought (Aug 9th), height of drought (Aug 31st), and recovery (Sep 8th) days.

On pre-drought (Aug 9th), temperature reached 29 °C during midday, whereas on drought (Aug 31st) and recovery (Sep 8th) days midday temperature reached 16 °C and 19 °C

respectively. Similarly, the daily height of outdoor PPFD was highest on pre-drought, second highest on recovery, and lowest on drought. During pre-drought outdoor PPFD varied greatly during sampling between approximately 600 and 2100 μmol·m^{-2}·s^{-1}. On drought and recovery outdoor PPFD during sampling was approximately 800-1300 and 900-1500 PPFD respectively. Indoor PPFD was recorded only during HSI measurement, according to which the brightest day indoors at the time of sampling was also pre-drought (315 μmol·m^{-2}·s^{-1}), followed by drought (121 μmol·m^{-2}·s^{-1}), and recovery (161 μmol·m^{-2}·s^{-1}). Comparability of variables dependent on environmental conditions between days suffer due to the differences in temperature and PPFD on the three sampling days. The days were chosen weeks in advance without knowledge of the dissimilar weather conditions due to time constraints and limited availability of shared instrumentation.

The development of LWP and F_v/F_m can be seen in the timeseries in Fig. 6. Treatment groups clearly differentiate for both variables and started to recover rabidly after regular watering was recommissioned. The drying of soil and recommission of watering is demonstrated in the relative soil moisture development timeseries available in Fig. A4 in Appendix 7.

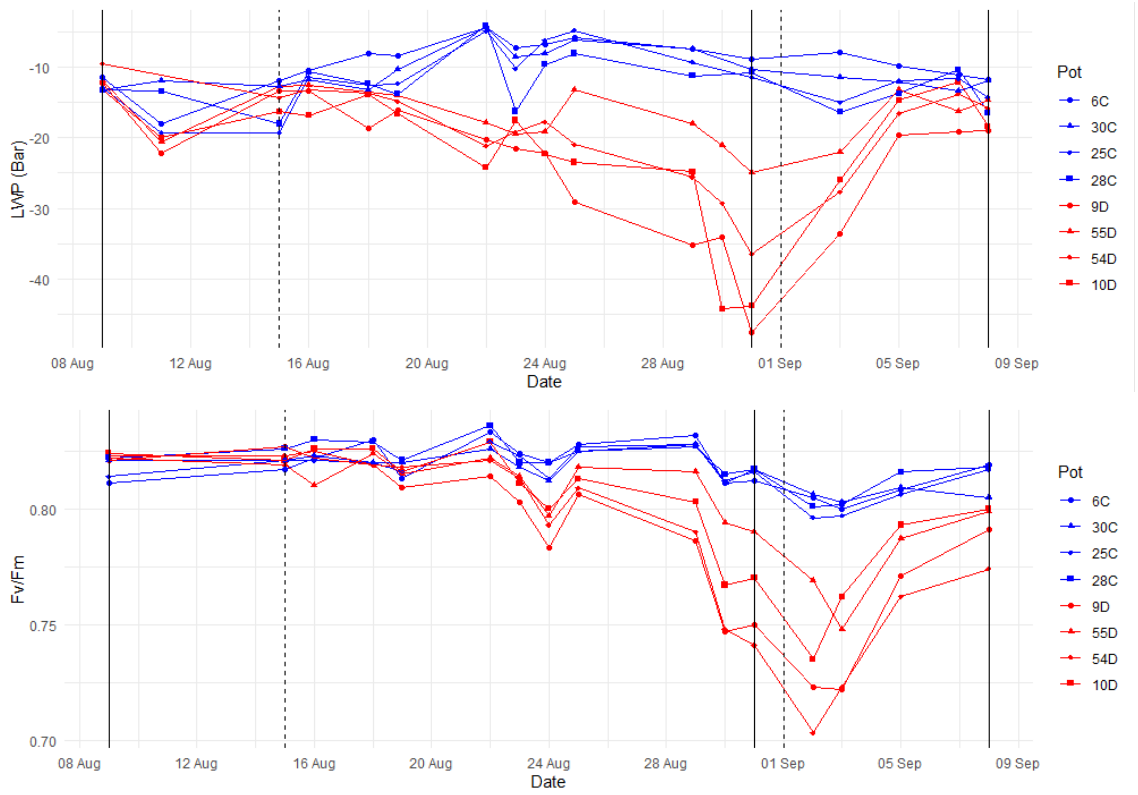

Figure 6. Timeseries of leaf water potential development in Bar (above), and F_v/F_m development (below). Control plants are denoted in blue and treatment plants in red. The black vertical lines denote the pre-drought (Aug 9th), height of drought (Aug 31st), and recovery (Sep 8th) days. The vertical dotted lines denote the start of drought treatment (Aug 17th) and recommission of irrigation (Sep 1st).

The differentiation of LWP values is further conveyed by the boxplot in Fig. 7 from pre-drought, drought, and recovery. On pre-drought and recovery, the difference between the distribution of LWP values between treatment and control groups is non-significant. Whereas, on drought the difference in distribution is significant with a 95% confidence level.

Fig. 8 depicts the distribution of F_v/F_m on the three primary sampling days. The difference is non-significant on pre-drought, but significant at a 95% confidence level on both drought and recovery. Based on visual assessment of the timeseries in Fig. 6 and the boxplots in Fig. 8, F_v/F_m-values seem to have started to recover but have not reached a fully recovered stable state equivalent of the control group. Whether full recovery was reached in terms of F_v/F_m following the treatment remains unknown.

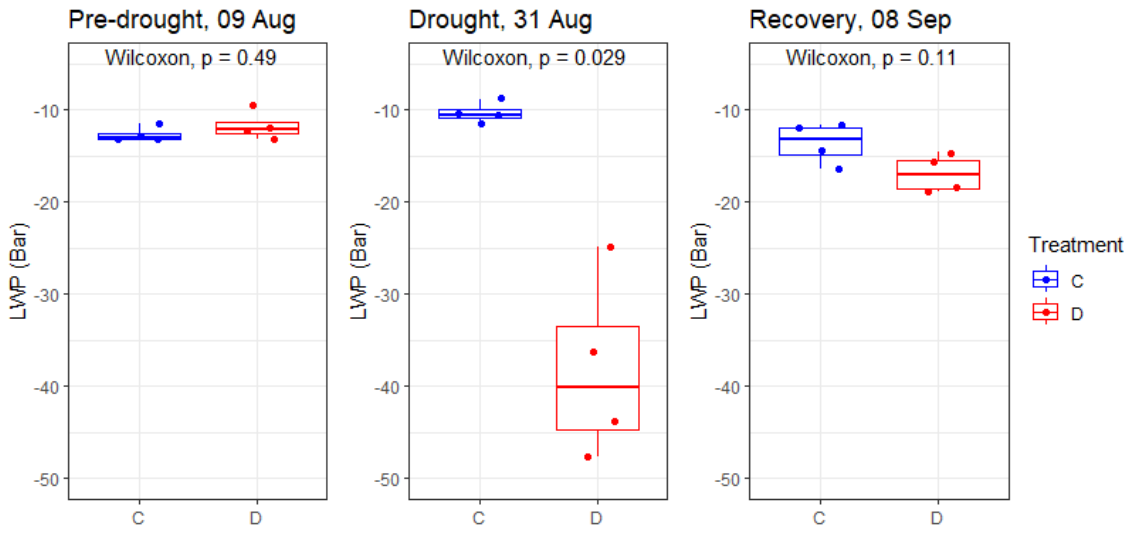

Figure 7. Boxplot depicting the spread of LWP values (Bar) of control (C) and drought (D) plants on three measuring days with Wilcoxon sum-rank test p-value between treatment groups calculated for each day.

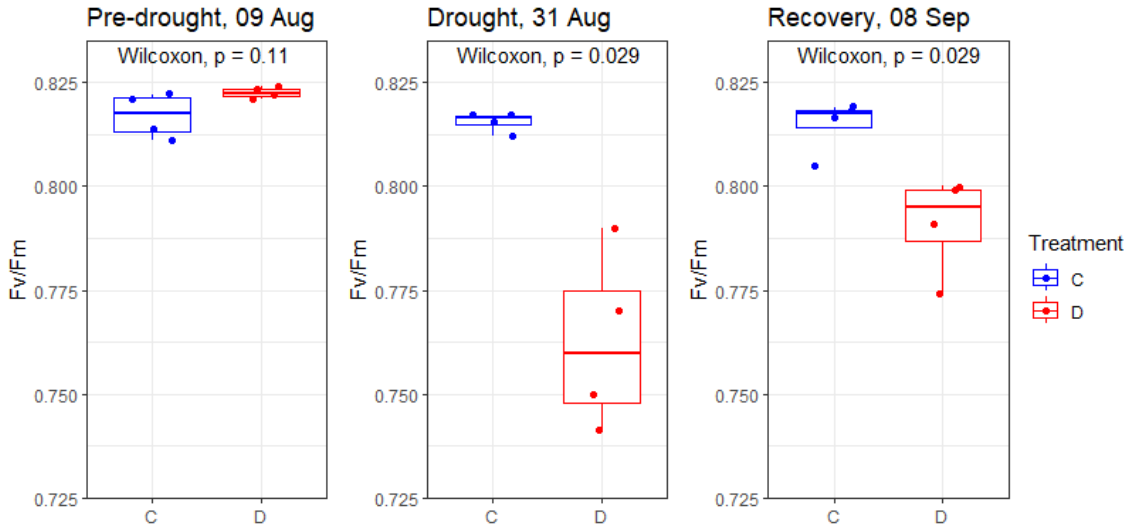

Figure 8. Boxplot depicting the spread of F_v/F_m of control (C) and drought (D) plants on three measuring days with Wilcoxon sum-rank test p-value between treatment groups calculated for each day.

PRI values based on leaf level reflectance (PRI_LL) attained with non-imaging-based spectroscopy are compared in Fig. 9. As expected, difference in PRI between treatment groups is non-significant on pre-drought and significant at a 95% confidence level on drought. On recovery, the difference is non-significant, but the overall spread and

skewness is dissimilar to the other two days, casting doubt on the validity of the reflectance data from that day. Leaf level reflectance curves can be seen in Fig. A5 in Appendix 8.

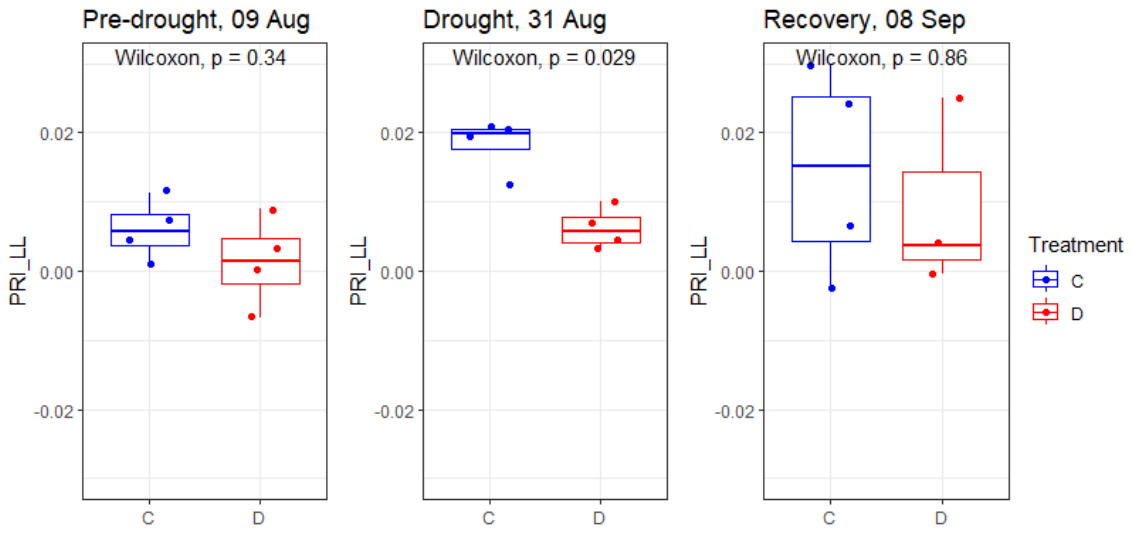

Figure 9. Boxplots depicting the spread of leaf level PRI of control (C) and drought (D) plants on three measuring days with Wilcoxon sum-rank test p-value between treatment groups calculated for each day.

3.2 HSI spectroscopy

Average HSI reflectance curve from each masked shoot area by date is available in Fig. 10. On recovery the NIR plateau was much higher compared to the other days, which suggests an error in illumination estimation on that day. The distribution of individual plant pixel reflectance curves is visualized in Fig. A8 in Appendix 9, which depicts the reflectance curves of 100 random pixels from the masked shoot areas. In Fig. 10, the red edge feature between approximately 680 and 750 nm seems somewhat similar between drought and control plants on pre-drought and drought. On recovery the red edge features of drought and control plants have seemingly differentiated. The graphs in the bottom row of Fig. 10 depict the reflectance in the 520-580 nm range. The shape of the feature in this range determines the value of PRI. Based on only visual estimation, the shape of this feature is similar between drought and control plants on pre-drought and recovery. On drought, the maximum peak of this feature has shifted towards longer wavelengths

for drought plants, being at around 555 nm, whereas for control plants it remains at approximately 550 nm.

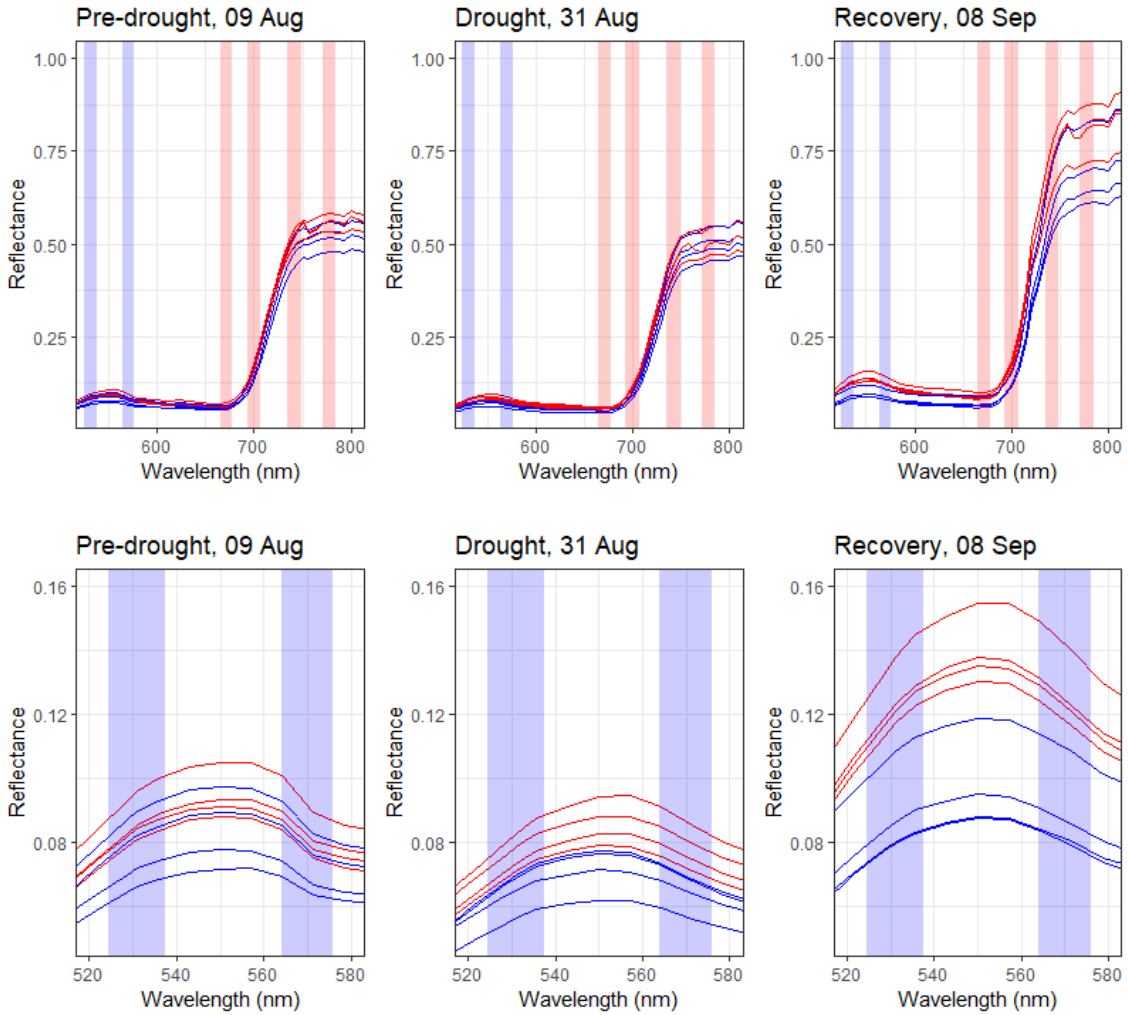

Figure 10. Full average HSI reflectance curve (above) and on the electromagnetic region used to calculate PRI (below) from masked shoot areas from the three primary sampling days. Control plant reflectance curves are in blue, and drought plant reflectance curves in red. The bands used to obtain PRI are demonstrated by the blue shaded areas and REP by the red shaded areas. The width of the shaded area correspond to the FWHM bandwidth of the signal.

3.2.1 PRI

Fig. 11 depicts the temporal and spatial development of HSI based PRI between the three days of measurement. In the bottom row images in Fig. 11, positive PRI values (indicating no stress) are displayed in purple and negative PRI values (indicating higher stress) in

orange. The difference between drought treatment and control plants during height of drought, with the slight exception of plant 55D, is evident in the bottom middle image of Fig. 11. Although there is a difference between the pre-drought and recovery images, both are clearly more homogenous in comparison to the drought image. The progression of PRI values is further illustrated in Fig. 12, in which the distribution of treatment group PRI values are compared within each day. As expected, PRI values of drought treated plants were highest on pre-drought, reached their minimum on drought, and increased again on recovery. The PRI values of control plants, on the other hand, decreased slightly over time. The difference in PRI distribution between groups is non-significant ($p > 0.05$) on pre-drought and recovery, and significant on drought ($p < 0.05$).

In addition to temporal changes in PRI, the HSI image (Fig. 11) reveals spatial differences within one plant. For example, there are visible differences between the needles of the primary shoot and side branches in some images. Although some differences can be accounted to scattering and overcast from surrounding objects, the effect is apparent in plant 30C pre-drought PRI image (Fig. 11, bottom left). These spatial differences are not quantified in this thesis, as the canopy-view is not appropriate for it. In the future, imaging plant profiles might reveal any differences due to position or age more reliably and clearly.

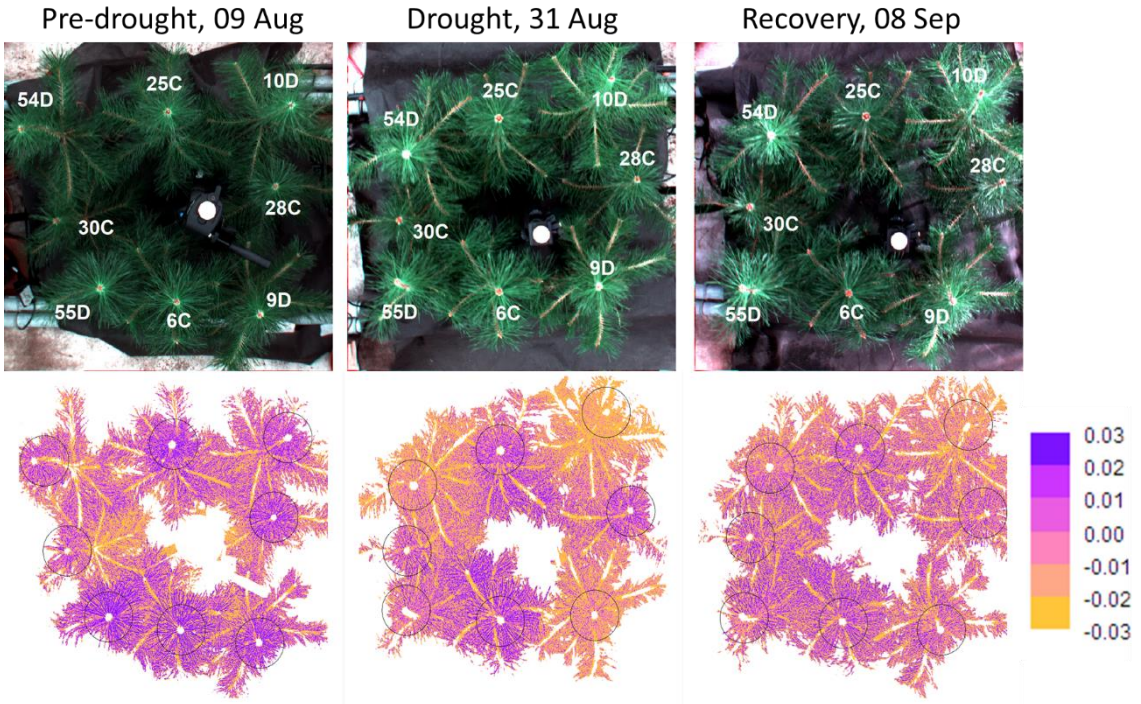

Figure 11. RGB images with tree ID labels (above) and corresponding PRI images (below) from the measuring days pre-drought (Aug 9th), drought (Aug 31st), and recovery (Sep 8th). Drought plants are identified with a 'D' and control plants with a 'C'. Black circles denote the limits of the circle mask and white pixels areas were NDVI < 0.7. The circular white panel used to gain the white reference spectra can be seen in the center of the RGB images. The black landscaping fabric used to minimize the effects of soil and other surrounding objects can also be seen in the background.

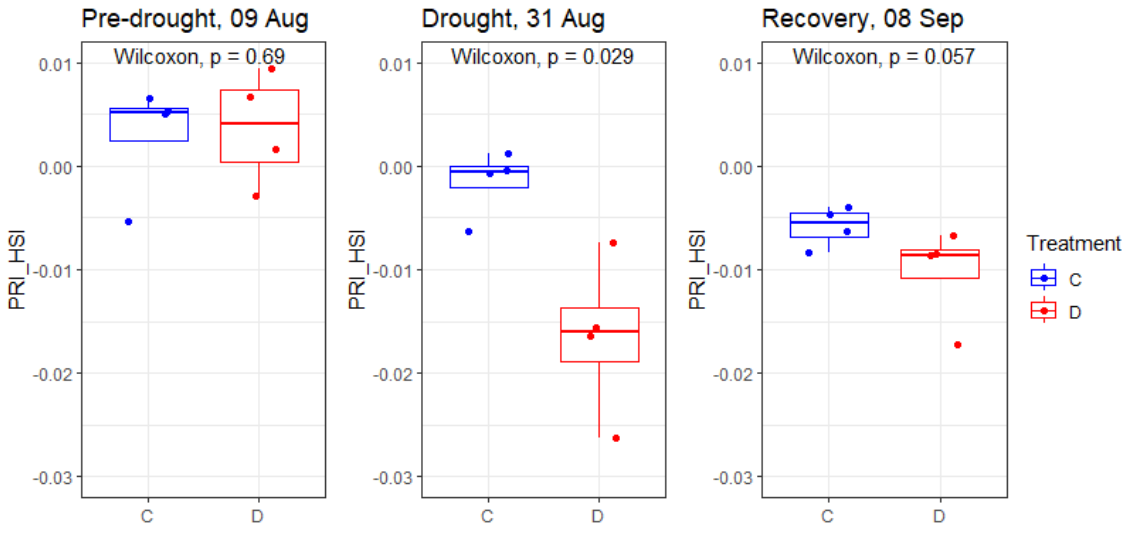

Figure 12. Boxplot depicting the spread of PRI values of control ('C') and drought ('D') plants on three measuring days with Wilcoxon sum-rank test p-value between treatment groups calculated for each day.

3.2.2 REP

Fig. 13 visualizes the temporal and spatial development of REP between the three days of measurement. Unlike PRI, REP is not uniform on pre-drought and recovery. On pre-drought, REPs of plants 54D, 30C, and 28C were positioned on longer wavelengths, which suggests a higher initial chlorophyll content. Regardless, these differences did not result in significant separation ($p > 0.05$) of treatment groups during pre-drought as can be seen in the first graph in Fig. 14. As demonstrated in the middle graph in Fig. 14, the distribution of REPs between treatment groups on drought is not significantly different ($p > 0.05$) due to one disparate value in the control group (plant 6C). On the other hand, on recovery, the difference is significant ($p < 0.05$). Comparing drought and recovery graphs in Fig. 13 and Fig. 14 confirm this increased polarization of REP values towards recovery. Similarly to PRI, REP values seemingly differ spatially between the primary shoot and branches within one plant. Like in the case of PRI, any affect of position or needle age on REP could be better assessed by imaging plants from side-view.

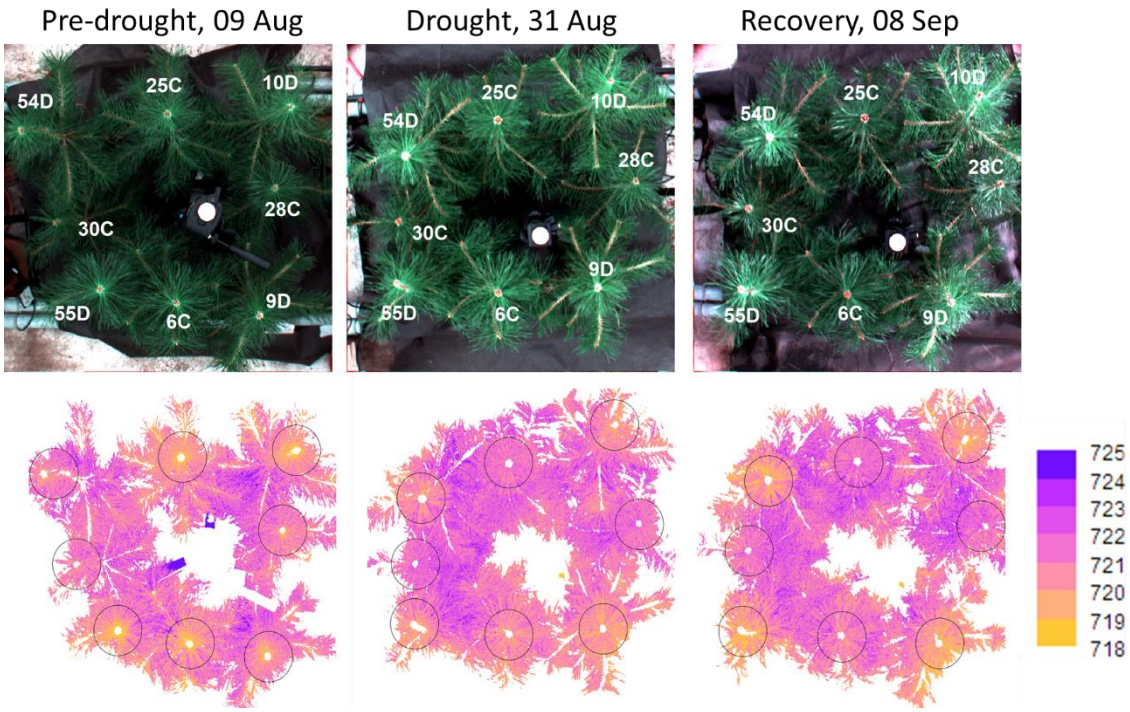

Figure 13. RGB images with tree labels (above) and corresponding REP (nm) images (below) from the measuring days pre-drought (Aug 9th), drought (Aug 31st), and recovery (Sep 8th). Drought plants are identified with a 'D' and control plants with a 'C'. Black circles denote the limits of the circle mask, and white pixels areas were NDVI < 0.7

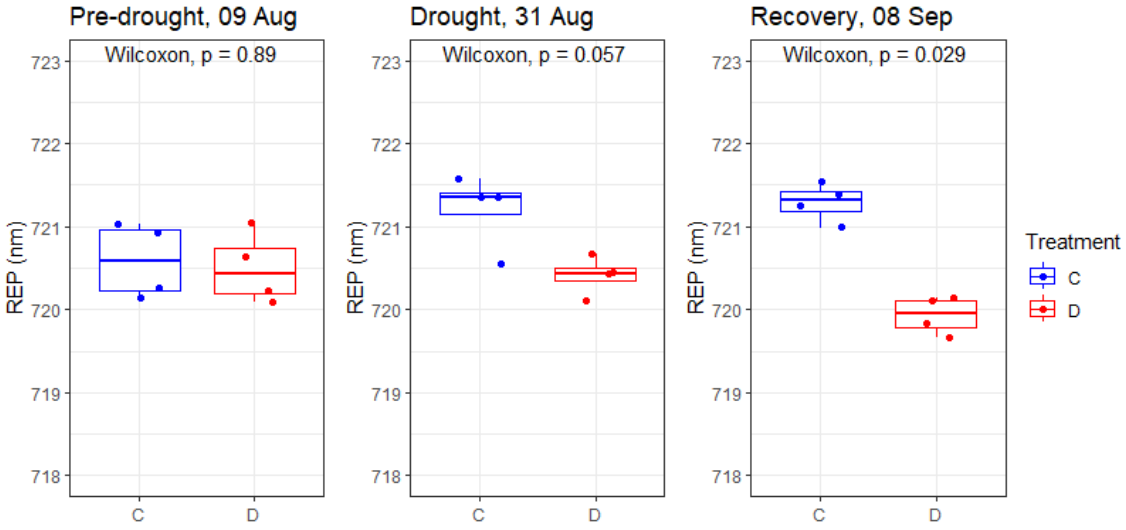

Figure 14. Boxplot depicting the spread of REP values of control ('C') and drought ('D') plants on three measurement days with Wilcoxon sum-rank test p-value between treatment groups calculated for each day.

3.3 Relationship between VIs and supporting variables

The linear relationships between PRI and LWP (Fig. 15 A), as well as PRI and F_v/F_m (Figure 15 B), were found to be significant ($p > 0.001$). PRI explained 55% and 49% of variance in LWP and F_v/F_m respectively. The relationship between REP and LWP (Figure 15 C) was significant at a 95% confidence level ($p = 0.041$) but explained only 13% of variance. The relationship between REP and F_v/F_m (Figure 15 D) was non-significant.

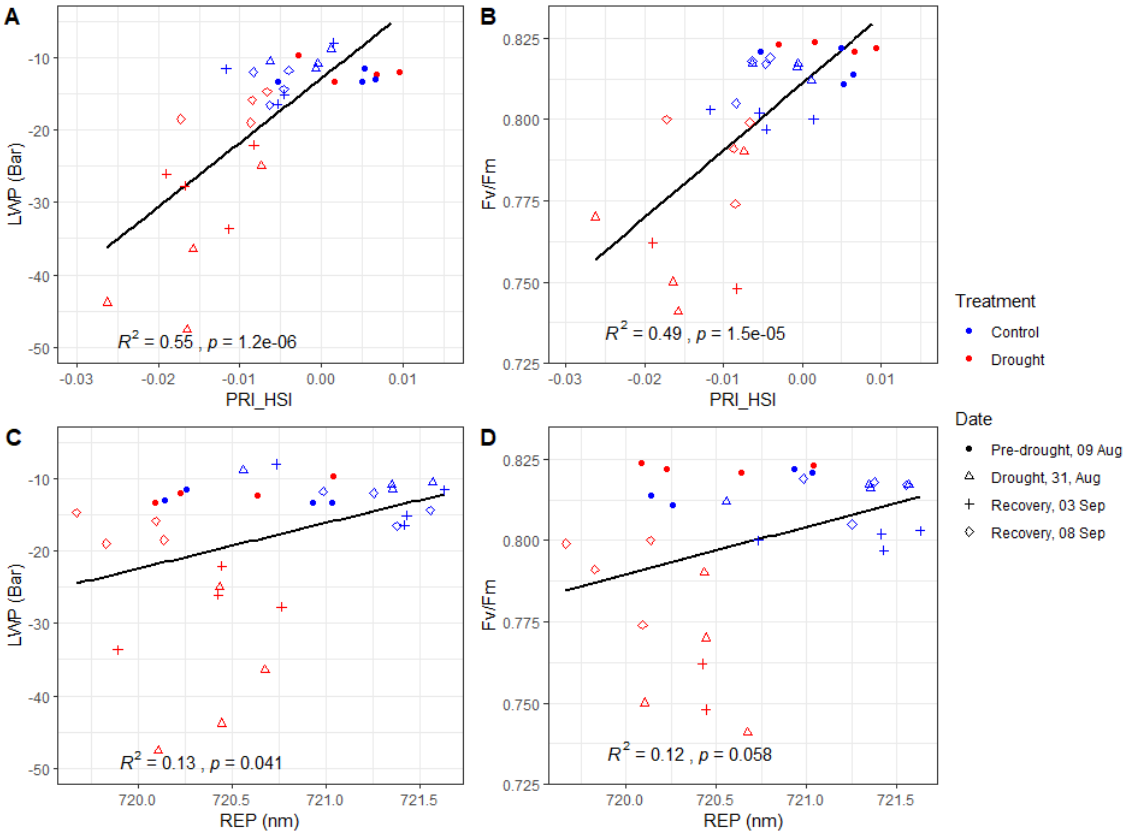

Figure 15. Relationship between A) PRI and LWP, B) PRI and F_v/F_m, C) REP and LWP, and D) REP and F_v/F_m.

Figure 16 summarizes the linear correlation between variables measured in this thesis by presenting a correlation matrix consisting of Pearson correlation coefficients (ρ). There was a strong significant positive correlation between LWP and F_v/F_m with HSI PRI (ρ = 0.74 and ρ = 0.69, respectively). The correlation of chlorophyll-based indexes REP and MERIS terrestrial chlorophyll index (MTCI) with supportive physiological variables LWP and F_v/F_m was not as strong as with HSI PRI, with ρ ranging from 0.36 to 0.48. The relationship between LWP and F_v/F_m with leaf level non-imaging PRI was non-significant and weak (ρ = .16 and ρ = .13). For further review of leaf level PRI relationship with supporting variables, linear regression is available in Fig. A6 in Appendix 9.

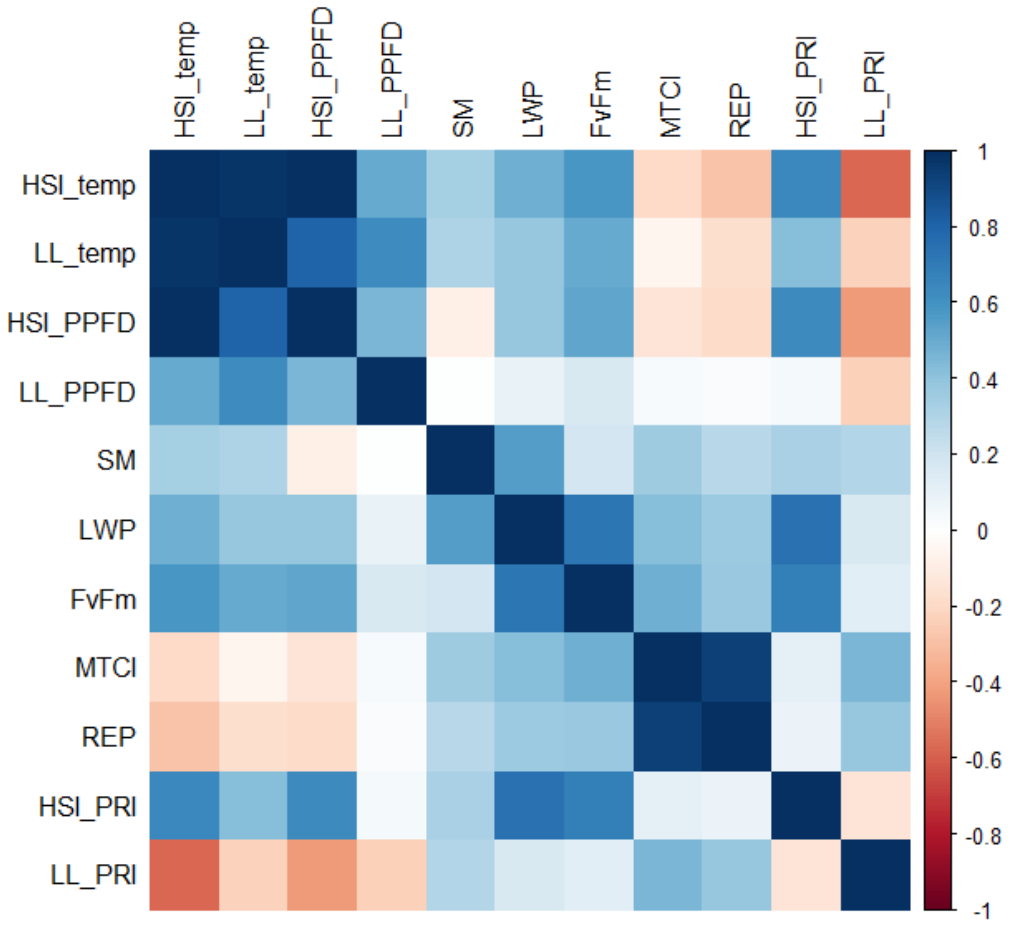

Figure 16. Pearson correlation coefficient matrix of VIs, and supporting and physiological variables. HSI_temp. is temperature (°C) at the time of HSI measurement, LL_temp. at the time of leaf level spectroscopy measurement. HSI_PPDF is PPFD ($\mu mol \cdot m^{-2} \cdot s^{-1}$) at the time of HSI, LL_PPFD at the time of leaf level spectroscopy. SM is relative soil moisture (%), LWP is leaf water potential (Bar), FvFm is maximum quantum yield of PSII photochemistry, MTCI is the MERIS terrestrial chlorophyll Index, REP is red edge position (nm), HSI_PRI is PRI from hyperspectral data, and LL_PRI is PRI from non-imaging-based leaf level reflectance.

Surprisingly, no relationship between PRI from HSI and leaf level spectroscopy was found (ρ = -.15, Figure 16), but in terms of the overall temporal pattern, the development of leaf level PRI (Fig. 9) was similar to that of HSI PRI (Fig. 12); the difference between treatment groups was non-significant on pre-drought and recovery, and significant on drought for both methods. Juxtaposed with HSI PRI values, leaf level PRI values were high and stably positive. A scatterplot matrix corresponding to Fig 16. may be found in Fig. A9 in Appendix 10.

4 DISCUSSION

4.1 Supporting and environmental variables

In comparison to previous studies on Scots pine, most of which have been concerned with winter downregulation or seasonal differences (Ottander and Oquist, 1991; Louis et al., 2005; Nichol et al., 2019), the drought treatment in this thesis led to a relatively small change in F_v/F_m, which was not sustained after rewatering. The relatively minor changes in Scots pine F_v/F_m induced by drought in comparison to seasonal changes coincides with previous research. Zlobin et al. (2019) reported the F_v/F_m values of 6-week-old Scots pine cultivates after 10 and 40 days of induced water stress by exposure to different nutrient water potentials (−1.5, −5, and –10 Bar) in water cultures. On the 10th day of treatment there was no differentiation between the treatment groups, but on the 40th treatment day the F_v/F_m values were 0.814, 0.704, and 0.660 from extreme to mild treatment condition. Perplexingly, the control treatment had the lowest F_v/F_m on the 10th day if treatment and remained lower than the mild water deficit treatment (-1.5 Bar) on the 40th day. In comparison, the seasonal minimum Fv/F_m of Scots pine has been reported to reach values sub 0.2 in late winter and early spring (Ottander et al., 1995.; Ottander and Oquist, 1991). Additionally in relation to LWP, F_v/F_m values in this thesis seem resistant to decline. Repo et al. (2005) reported LWP alongside F_v/F_m in a spring soil thawing experiment. In the study by Repo et al. (2005) F_v/F_m approached 0 as LWP reached -20 Bar. Regardless, declining F_v/F_m-values in general indicated increased energy dissipation by NPQ (Bolhar-Nordenkampf et al., 1989), and as F_v/F_m-development within this thesis was consistent with treatment group (Fig. 8) and treatment progression (Fig. 6), it can be affirmed that the treatment was successful in inducing drought stress, which led to physiological changes.

LWP values are aligned with the development of F_v/F_m in the sense that they are consisted with treatment group (Fig. 7) and treatment progression (Fig. 6). However, LWP values measured for this thesis cause concern for being consistently lower in comparison to the level set by previous studies. Minimum LWP of control trees in this thesis ranged between -19.3 and -18.1 Bar, whereas Irvine et al. (1998) reported analogous values between -11.9

and -6.8 Bar measured from 41-year-old Scots pine in field conditions between July and September 1995. Minimum LWP for drought treated plants in this thesis was between -47 and -25 Bar, whereas Irvine et al. (1998) reported a range of -14.1 to -10.8 Bar. Other studies have generally reported minimum LWP values ranging from -25 to -20 Bar for Scots pine (Martínez-Vilalta et al., 2009; Poyatos et al., 2013). Repo et al. (2005) reported a Scots pine needle recovery threshold between -17 and -15 Bar in a study following the effects of soil thawing in the spring, but notes that conifers have been observed to recover from lower LWPs and that the cause of death was likely influenced by other factors. In a study concerned with conifer die-off caused by drought, Breshears et al. (2009) reported the death of all four *Pinus edulis* pine trees after sustaining LWP below -20 Bar for 10 months. It is therefore open to question whether the drought treated pines in this thesis would have been able to survive LWP values recorded at height of drought even though the condition was temporary. On the other hand, Breshears et al. (2009) includes a *Pinus edulis* that recover after LWP dipped close to -40 Bar in 1998 and survived for another 4 years. Additionally, they also reported a *Pinus edulis* temporarily recovering after LWP dipped below -50 Bar in 2002, but then proceeding to die within a year.

Although LWP values reported in this thesis may be reliable, previous studies indicate that they might be concerningly low across both groups (Irvine et al., 1998; Martínez-Vilalta et al., 2009; Poyatos et al., 2013; Repo et al., 2005). This could have resulted from a number of systematic errors resulting from improper use of instrument, observation bias, or faulty equipment (such as a leaking valve). To my knowledge, LWP from drought stressed current year needles of Scots pine seedlings have not been published and cannot be utilized here for direct comparison.

Weather in terms of temperature and PPFD varied greatly between the three main measuring days, with the pre-drought date (Aug 9th) being the hottest and brightest (Fig. 5). As light conditions being excessive or limiting are the driving cause of dynamics in the xanthophyll cycle (Gamon et al., 1992), absolute PRI values between-days are not comparable. The uneven weather conditions may explain the differences between absolute PRI values of control group plants between-days.

4.2 Spectroscopy

The offset of leaf level PRI in comparison to HSI PRI, lack of correlation with HSI PRI and supporting variables, and wide distribution of leaf level PRI of pre-drought might be due to natural diurnal changes in PRI (Gamon et al., 1992). Leaf level measurements were time consuming and were taken within a time frame of approximately 3 hours. Graphs of time and meteorological conditions for leaf level reflectance measurements are available in Fig. A6 in Appendix 6. Other sampling and HSI were collected in a shorter time frame at midday, which coincides with minimal diurnal PRI (Gamon et al., 2015). Due to the diurnal cycle, and changes in meteorological conditions, leaf level data suffers from the same limitation as between-days comparison, and cannot, in this thesis, be used as validation for HSI PRI. In this experimental setting, the main advantage of HSI over the leaf level non-imaging approach was that measurements of all plants could be taken simultaneously in the exact same diurnal conditions. Additionally, the leaf level data collection was done under a strong LED-light that was not representative of the low PPFD condition in the shaded greenhouse. This, and the fact that needles were not accumulated to the measuring cuvette likely contributed to the discrepancy between HSI and leaf level PRI.

Unlike leaf level PRI, HSI PRI was found to significantly correlate with the physiological variables LWP and F_v/F_m, accounting for 55 and 49% of variation respectively (Fig. 15 A and B). This result coincides with previous knowledge on water stress affecting the level on which light is excessive, increasing the plant's need of energy dissipation via the xanthophyll cycle (Demmig-Adams and Adams, 1996; Zhang et al., 2017), which PRI is based on (Gamon et al., 1992).

The HSI based PRI could capture response to water stress during drought and recovery, as is evident by significant difference between the control and drought plants during drought, and non-significant difference during pre-drought and recovery (Fig. 11 and Fig. 12). It is likely that the changes in PRI are indeed due to reversible photoprotective energy dissipation in the xanthophyll cycle, as short term shifts are associated with it, whereas long term seasonal patterns are correlated with the overall chlorophyll-

carotenoid pigment ratio (Gamon et al., 2015). This could be confirmed with knowledge of the EPS of xanthophyll cycle pigments in the samples. Pigment samples were collected during this experiment, but as they were sent for analysis externally, results are not available as of now. Once pigment assay results have been received and analyzed, it can be asserted with confidence whether the decline and recovery in PRI was due to the dynamics of the xanthophyll cycle.

In the experimental setting of this thesis, PRI outperformed chlorophyll-based REP in capturing response to stress; REP's response to drought development was delayed in comparison to PRI, and it did not show signs of recovery (Fig. 14). As a result, REP did not model the development of supporting physiological variables as well as PRI. Affirmingly, Imanishi et al. (2004) also concluded that REP was not useful in detecting drought in oak species on a canopy level. On the other hand, they suggested that the wavelengths at the beginning of the red edge feature were better at detecting water status variables. For example, Zhang et al. (2017) used the ratio R_{690}/R_{630}, which overlaps with the initial slope of the red edge, successfully to monitor drought and photosynthetic recovery in evergreen oak seedlings. Moreover, in a recent publication Genangeli et al. (2023) applied the same Senop HSI camera as used in this thesis in identifying drought resistant tomato phenotypes based on an index related to the red edge. Nevertheless, the REP values reported in this thesis suggests that chlorophyll content decreased in drought trees. This coincides with previous research. Zlobin et al. (2019) reported decrease in photosynthetic pigments, including chlorophyll a and b, and total carotenoid pool, in response to drought. They suggested that the suppression of photosynthetic pigments may be a way of preventing excessive light absorption and formation of reactive oxygen species, which cause photodamage.

4.3 Limitations and future prospects of HSI

There are several limitations to the HSI results of this thesis resulting from operating solely on factory calibration, and difficulty of measuring complex plant architecture in uneven ambient light conditions. Most of these issues provide opportunities for improving HSI protocol in the future.

4.3.1 HSI camera calibrations

The results of this thesis are limited by the lack of calibration done prior to the start of the campaign. Calibration procedures that could be included in future studies using the same instrument are spectral calibration and flat-field calibration (Qin et al., 2013; Kokka et al., 2019).

Spectral calibration can be done using a lamp generating illumination on known narrow wavelength bands, and by correlating the signals detected by the camera to those wavelengths. Narrow spectral signals in calibration lambs can be generated from the excitation of specific gases like argon, krypton, neon, xenon, or mercury (Qin et al., 2013). Conducting spectral calibration provides certainty that bands selected for an imaging protocol are truly representative of the desired wavelengths. Spectral features, including those used in this thesis to calculate VIs, are often narrow, and an offset in band position can lead to distortion of results. Spectral calibration using a monochromator can also be utilized to determine the true bandwidth of the camera's bands in certain ranges. The exact FWHM bandwidths used by the camera are reported to be between 11 and 19 (Table A3 in Appendix 5), but they have not been confirmed. Regardless, even at its narrowest, the bandwidth used by the camera is relatively wide, which inevitably leads to some level of signal mixing.

Flat-field calibration is performed to determine spatial variation in responsivity to radiation (Kokka et al., 2019). In imaging there generally exists a radial fall-off effect caused by angular sensitivity of perceived radiation intensity towards the edges of the image. This results in vignetting. Vignetting is also contributed to by physical elements interfering with radiation at the edge of the field of view (Goldman, 2010). Flat-field correction is done by calculating a correction matrix corresponding to each pixel, and by transforming the raw data cube by that matrix. The correction matrix is based on imaging a uniform source of radiance. This could be done by imaging an integrating sphere or a white panel under controlled light conditions (Kokka et al., 2019).

4.3.2 White panel

The white panel used in this thesis to estimate maximum signal for reflectance calculation was a flat surface and did therefore not account for the complex 3D-structure of the pines and the irradiance received by those irregular surfaces. The white panel was also set at the median height of the canopy, so that some shoots were slightly above or below it. Distance from the sensor to needles was therefore different than to the white panel (Table A2 in Appendix 4). Additionally, surrounding canopy and architecture of plants impact interaction with illumination, although a black landscaping fiber cloth was used over the pots and surrounding ground to minimize some of these effects. Regardless, all these factors cause unaccounted distortions, which affects the amount of measured received radiance (Behmann et al., 2016; Paulus and Mahlein, 2020). Normalization by distance has been suggested as a solution to this issue. This could be done by integrating 3D shape information (e.g,. via laser scanning) to HSI images (Behmann et al., 2016; Mishra et al., 2020; Paulus and Mahlein, 2020).

4.3.3 Automation of HSI

Automation of the HSI imaging protocol would allow for more efficient and easy long-term data collection in follow-up studies that might monitor drought development or differences in population drought response in the wild. Automation of imaging would also be a prerequisite for including the Senop HSC-2 camera in a drone, or permanently placing it in a measuring tower. Both are possible approached to expanding the scale of this thesis' experimental setting to forest stand level. Some issues related to automation that need to be solved before are data storage, dark current automation, and selection of integration time. Additionally, for use outside of the greenhouse the camera needs to be weather-proofed.

HSI data cubes are large, and the internal memory of the camera is only 2 terabytes. If data is collected for an extended period at set time intervals, the memory will not be sufficient, and an alternative storage where data can reliably be transferred needs to be

established. The large amount of data will also be a challenge during analysis, which could for example be done using high-performance computing.

Some spectroscopic instruments have an automatic internal shutter for measuring the dark current, but the HSI camera used in this thesis does not. The dark current was thus acquired by covering the lens with a detachable lens cap provided with the camera. An external shutter or cap system needs to be developed for the automatic acquisition of the dark current. For this thesis, integration time was set manually with the aid of a PPFD sensor. This process could be automated by for example setting irradiance ranges for specific integration times. The camera's manufacturer offers a relative irradiance sensor accessory to the camera, which measures current radiation flow level in W/m^3. This could be incorporated to the automatic setting of integration time.

5 CONCLUSIONS

This thesis assessed the feasibility of measuring VIs of Scots pine seedlings on a canopy level in greenhouse conditions using HSI, and whether HSI based PRI can be utilized in monitoring Scots pine seedling drought stress development and recovery in these conditions. The data was collected in August and September 2022, and consisted of HSI images of drought treated and control seedlings from pre-drought, drought, and recovery periods, leaf level reflectance from a non-imaging spectrometer, meteorological data, and supporting physiological variables LWP and F_v/F_m.

The temporal development and significant difference supporting physiological variables LWP and F_v/F_m between treatment groups indicated that the drought treatment was successful in inducing drought response in the treatment plants. The relationship between HSI based PRI and physiological variables was significant. PRI responded to drought development and recovery, which is expected to be due to reversible photoprotective energy dissipation by the xanthophyll cycle. Pending analysis of pigment samples and knowledge of EPS will confirm this. Chlorophyll-based VI REP captured drought development but did not respond to recovery. The relationship between physiological variables and REP was either non-significant or minor. Regardless, the results of this

thesis demonstrated that HSI is a promising tool in remote sensing plant properties and functions. Further refinement of HSI methodology and full automation is still needed, but HSI can be applied in drought monitoring.

6 REFERENCES

Alonso Chorda, L. 2023. Personal communication, 2023. Doctor, Researcher, Optics of Photosynthesis Lab, Univ. of Helsinki, Finland.

Behmann, J., Mahlein, A.-K., Paulus, S., Dupuis, J., Kuhlmann, H., Oerke, E.-C., Plümer, L., 2016. Generation and application of hyperspectral 3D plant models: methods and challenges. Mach. Vis. Appl. 27, 611–624. https://doi.org/10.1007/s00138-015-0716-8

Bolhar-Nordenkampf, H.R., Long, S.P., Baker, N.R., Oquist, G., Schreiber, U., Lechner, E.G., 1989. Chlorophyll Fluorescence as a Probe of the Photosynthetic Competence of Leaves in the Field: A Review of Current Instrumentation. Funct. Ecol. 3, 497. https://doi.org/10.2307/2389624

Breshears, D.D., Myers, O.B., Meyer, C.W., Barnes, F.J., Zou, C.B., Allen, C.D., McDowell, N.G., Pockman, W.T., 2009. Tree die-off in response to global change-type drought: mortality insights from a decade of plant water potential measurements. Front. Ecol. Environ. 7, 185–189. https://doi.org/10.1890/080016

Carvalho, R.F., Takaki, M., Azevedo, R.A., 2011. Plant pigments: the many faces of light perception. Acta Physiol. Plant. 33, 241–248. https://doi.org/10.1007/s11738-010-0533-7

Cho, M.A., Skidmore, A.K., 2006. A new technique for extracting the red edge position from hyperspectral data: The linear extrapolation method. Remote Sens. Environ. 101, 181–193. https://doi.org/10.1016/j.rse.2005.12.011

Chuvieco, E., Aguado, I., Salas, J., García, M., Yebra, M., Oliva, P., 2020. Satellite Remote Sensing Contributions to Wildland Fire Science and Management. Curr. For. Rep. 6, 81–96. https://doi.org/10.1007/s40725-020-00116-5

Demmig-Adams, B., 1990. Carotenoids and photoprotection in plants: A role for the xanthophyll zeaxanthin. Biochim. Biophys. Acta BBA - Bioenerg. 1020, 1–24. https://doi.org/10.1016/0005-2728(90)90088-L

Demmig-Adams, B., Adams, W.W., 1996. The role of xanthophyll cycle carotenoids in the protection of photosynthesis. Trends Plant Sci. 1, 21–26. https://doi.org/10.1016/S1360-1385(96)80019-7

D'Odorico, P., Schönbeck, L., Vitali, V., Meusburger, K., Schaub, M., Ginzler, C., Zweifel, R., Velasco, V.M.E., Gisler, J., Gessler, A., Ensminger, I., 2021. Drone-based physiological index reveals long-term acclimation and drought stress responses in trees. Plant Cell Environ. 44, 3552–3570. https://doi.org/10.1111/pce.14177

Ensminger, I., 2020. Fast track diagnostics: hyperspectral reflectance differentiates disease from drought stress in trees. Tree Physiol. 40, 1143–1146. https://doi.org/10.1093/treephys/tpaa072

Feng, X., Zhan, Y., Wang, Q., Yang, X., Yu, C., Wang, H., Tang, Z., Jiang, D., Peng, C., He, Y., 2020. Hyperspectral imaging combined with machine learning as a tool to obtain high-throughput plant salt-stress phenotyping. Plant J. 101, 1448–1461. https://doi.org/10.1111/tpj.14597

Féret, J.-B., Berger, K., de Boissieu, F., Malenovský, Z., 2021. PROSPECT-PRO for estimating content of nitrogen-containing leaf proteins and other carbon-based constituents. Remote Sens. Environ. 252, 112173. https://doi.org/10.1016/j.rse.2020.112173

Filella, I., Penuelas, J., 1994. The red edge position and shape as indicators of plant chlorophyll content, biomass and hydric status. Int. J. Remote Sens. 15, 1459–1470. https://doi.org/10.1080/01431169408954177

Gamon, J.A., Field, C.B., Bilger, W., Björkman, O., Fredeen, A.L., Penuelas, J., 1990. Remote sensing of the xanthophyll cycle and chlorophyll fluorescence in sunflower leaves and canopies.

Gamon, J.A., Kovalchuck, O., Wong, C.Y.S., Harris, A., Garrity, S.R., 2015. Monitoring seasonal and diurnal changes in photosynthetic pigments with automated PRI and

NDVI sensors. Biogeosciences 12, 4149–4159. https://doi.org/10.5194/bg-12-4149-2015

Gamon, J.A., Penuelas, J., Field, C.B., 1992. A Narrow-Waveband Spectral Index That Tracks Diurnal Changes in Photosynthetic Efficiency.

Genty, B., Briantais, J.-M., Baker, N.R., 1989. The relationship between the quantum yield of photosynthetic electron transport and quenching of chlorophyll fluorescence. Biochim. Biophys. Acta BBA - Gen. Subj. 990, 87–92. https://doi.org/10.1016/S0304-4165(89)80016-9

Goldman, D.B., 2010. Vignette and Exposure Calibration and Compensation. IEEE Trans. Pattern Anal. Mach. Intell. 32, 2276–2288. https://doi.org/10.1109/TPAMI.2010.55

Guyot, G., Baret, F., 1988. Utilisation de la Haute Resolution Spectrale pour Suivre L'etat des Couverts Vegetaux 287, 279.

Imanishi, J., Sugimoto, K., Morimoto, Y., 2004. Detecting drought status and LAI of two Quercus species canopies using derivative spectra. Comput. Electron. Agric. 43, 109–129. https://doi.org/10.1016/j.compag.2003.12.001

Irvine, J., Perks, M.P., Magnani, F., Grace, J., 1998. The response of Pinus sylvestris to drought: stomatal control of transpiration and hydraulic conductance. Tree Physiol. 18, 393–402. https://doi.org/10.1093/treephys/18.6.393

Khan, M.J., Khan, H.S., Yousaf, A., Khurshid, K., Abbas, A., 2018. Modern Trends in Hyperspectral Image Analysis: A Review. IEEE Access 6, 14118–14129. https://doi.org/10.1109/ACCESS.2018.2812999

Kokka, A., Pulli, T., Honkavaara, E., Markelin, L., Kärhä, P., Ikonen, E., 2019. Flat-field calibration method for hyperspectral frame cameras. Metrologia 56, 055001. https://doi.org/10.1088/1681-7575/ab3261

Louis, J., Ounis, A., Ducruet, J.-M., Evain, S., Laurila, T., Thum, T., Aurela, M., Wingsle, G., Alonso, L., Pedros, R., Moya, I., 2005. Remote sensing of sunlight-induced

chlorophyll fluorescence and reflectance of Scots pine in the boreal forest during spring recovery. Remote Sens. Environ. 96, 37–48. https://doi.org/10.1016/j.rse.2005.01.013

Martínez-Vilalta, J., Cochard, H., Mencuccini, M., Sterck, F., Herrero, A., Korhonen, J.F.J., Llorens, P., Nikinmaa, E., Nolè, A., Poyatos, R., Ripullone, F., Sass-Klaassen, U., Zweifel, R., 2009. Hydraulic adjustment of Scots pine across Europe. New Phytol. 184, 353–364. https://doi.org/10.1111/j.1469-8137.2009.02954.x

Mishra, P., Lohumi, S., Ahmad Khan, H., Nordon, A., 2020. Close-range hyperspectral imaging of whole plants for digital phenotyping: Recent applications and illumination correction approaches. Comput. Electron. Agric. 178, 105780. https://doi.org/10.1016/j.compag.2020.105780

Mitchell, P.J., O'Grady, A.P., Tissue, D.T., White, D.A., Ottenschlaeger, M.L., Pinkard, E.A., 2013. Drought response strategies define the relative contributions of hydraulic dysfunction and carbohydrate depletion during tree mortality. New Phytol. 197, 862–872. https://doi.org/10.1111/nph.12064

Nichol, C., Drolet, G., Porcar-Castell, A., Wade, T., Sabater, N., Middleton, E., MacLellan, C., Levula, J., Mammarella, I., Vesala, T., Atherton, J., 2019. Diurnal and Seasonal Solar Induced Chlorophyll Fluorescence and Photosynthesis in a Boreal Scots Pine Canopy. Remote Sens. 11, 273. https://doi.org/10.3390/rs11030273

Ottander, C., Campbell, D., Oquist, G., 1995. Seasonal changes in photosystem II organisation and pigment composition in Pinus syivestris.

Ottander, C., Oquist, G., 1991. Recovery of photosynthesis in winter-stressed Scots pine. Plant Cell Environ. 14, 345–349. https://doi.org/10.1111/j.1365-3040.1991.tb01511.x

Paulus, S., Mahlein, A.-K., 2020. Technical workflows for hyperspectral plant image assessment and processing on the greenhouse and laboratory scale. GigaScience 9, giaa090. https://doi.org/10.1093/gigascience/giaa090

Pettorelli, N., Vik, J.O., Mysterud, A., Gaillard, J.-M., Tucker, C.J., Stenseth, N.Chr., 2005. Using the satellite-derived NDVI to assess ecological responses to environmental change. Trends Ecol. Evol. 20, 503–510. https://doi.org/10.1016/j.tree.2005.05.011

Porcar-Castell, A., Tyystjärvi, E., Atherton, J., van der Tol, C., Flexas, J., Pfündel, E.E., Moreno, J., Frankenberg, C., Berry, J.A., 2014. Linking chlorophyll a fluorescence to photosynthesis for remote sensing applications: mechanisms and challenges. J. Exp. Bot. 65, 4065–4095. https://doi.org/10.1093/jxb/eru191

Poyatos, R., Aguadé, D., Galiano, L., Mencuccini, M., Martínez-Vilalta, J., 2013. Drought-induced defoliation and long periods of near-zero gas exchange play a key role in accentuating metabolic decline of Scots pine. New Phytol. 200, 388–401. https://doi.org/10.1111/nph.12278

Qin, J., Chao, K., Kim, M.S., Lu, R., Burks, T.F., 2013. Hyperspectral and multispectral imaging for evaluating food safety and quality. J. Food Eng. 118, 157–171. https://doi.org/10.1016/j.jfoodeng.2013.04.001

R Core Team. 2023. R: A language and environment for statistical computing. R Foundation for Statistical Computing, Vienna, Austria. Available: https://www.R-project.org/ [Accessed 21 May 2023].

Repo, T., Kalliokoski, T., Domisch, T., Lehto, T., Mannerkoski, H., Sutinen, S., Finer, L., 2005. Effects of timing of soil frost thawing on Scots pine. Tree Physiol. 25, 1053–1062. https://doi.org/10.1093/treephys/25.8.1053

Ripullone, F., Rivelli, A.R., Baraldi, R., Guarini, R., Guerrieri, R., Magnani, F., Peñuelas, J., Raddi, S., Borghetti, M., 2011. Effectiveness of the photochemical reflectance index to track photosynthetic activity over a range of forest tree species and plant water statuses. Funct. Plant Biol. 38, 177. https://doi.org/10.1071/FP10078

Roy, P.S., 1989. Spectral reflectance characteristics of vegetation and their use in estimating productive potential. Proc. Indian Acad. Sci. (Plant Sci.) 99, 58–81. https://doi.org/10.1007/BF03053419

Sarić, R., Nguyen, V.D., Burge, T., Berkowitz, O., Trtílek, M., Whelan, J., Lewsey, M.G., Čustović, E., 2022. Applications of hyperspectral imaging in plant phenotyping. Trends Plant Sci. 27, 301–315. https://doi.org/10.1016/j.tplants.2021.12.003

Scholander, P.F., Bradstreet, E.D., Hemmingsen, E.A., Hammel, H.T., 1965. Sap Pressure in Vascular Plants: Negative hydrostatic pressure can be measured in plants. Science 148, 339–346. https://doi.org/10.1126/science.148.3668.339

Schreiber, U., Schliwa, U., Bilger, W., 1986. Continuous recording of photochemical and non-photochemical chlorophyll fluorescence quenching with a new type of modulation fluorometer. Photosynth. Res. 10, 51–62. https://doi.org/10.1007/BF00024185

Semerci, A., Semerci, H., Çalişkan, B., Çiçek, N., Ekmekçi, Y., Mencuccini, M., 2017. Morphological and physiological responses to drought stress of European provenances of Scots pine. Eur. J. For. Res. 136, 91–104. https://doi.org/10.1007/s10342-016-1011-6

Suárez, L., Zarco-Tejada, P.J., Sepulcre-Cantó, G., Pérez-Priego, O., Miller, J.R., Jiménez-Muñoz, J.C., Sobrino, J., 2008. Assessing canopy PRI for water stress detection with diurnal airborne imagery. Remote Sens. Environ. 112, 560–575. https://doi.org/10.1016/j.rse.2007.05.009

Tyree, M.T., 2003. Hydraulic limits on tree performance: transpiration, carbon gain and growth of trees. Trees 17, 95–100. https://doi.org/10.1007/s00468-002-0227-x

Watt, M.S., Leonardo, E.M.C., Estarija, H.J.C., Massam, P., de Silva, D., O'Neill, R., Lane, D., McDougal, R., Buddenbaum, H., Zarco-Tejada, P.J., 2021. Long-term effects of water stress on hyperspectral remote sensing indicators in young radiata pine. For. Ecol. Manag. 502, 119707. https://doi.org/10.1016/j.foreco.2021.119707

Wong, C.Y.S., D'Odorico, P., Arain, M.A., Ensminger, I., 2020. Tracking the phenology of photosynthesis using carotenoid-sensitive and near-infrared reflectance vegetation indices in a temperate evergreen and mixed deciduous forest. New Phytol. 226, 1682–1695. https://doi.org/10.1111/nph.16479

Wong, C.Y.S., Gamon, J.A., 2015. The photochemical reflectance index provides an optical indicator of spring photosynthetic activation in evergreen conifers. New Phytol. 206, 196–208. https://doi.org/10.1111/nph.13251

Xue, J., Su, B., 2017. Significant Remote Sensing Vegetation Indices: A Review of Developments and Applications. J. Sens. 2017, 1–17. https://doi.org/10.1155/2017/1353691

Yamamoto, H.Y., 1979. Biochemistry of the violaxanthin cycle in higher plants. Pure Appl. Chem. 51, 639–648. https://doi.org/10.1351/pac197951030639

Yamamoto, H.Y., Kamite, L., 1972. The effects of dithiothreitol on violaxanthin de-epoxidation and absorbance changes in the 500-nm region. Biochim. Biophys. Acta BBA - Bioenerg. 267, 538–543. https://doi.org/10.1016/0005-2728(72)90182-X

Yang, J.C., Magney, T.S., Yan, D., Knowles, J.F., Smith, W.K., Scott, R.L., Barron-Gafford, G.A., 2020. The Photochemical Reflectance Index (PRI) Captures the Ecohydrologic Sensitivity of a Semiarid Mixed Conifer Forest. J. Geophys. Res. Biogeosciences 125. https://doi.org/10.1029/2019JG005624

Zahir, S.A.D.M., Omar, A.F., Jamlos, M.F., Azmi, M.A.M., Muncan, J., 2022. A review of visible and near-infrared (Vis-NIR) spectroscopy application in plant stress detection. Sens. Actuators Phys. 338, 113468. https://doi.org/10.1016/j.sna.2022.113468

Zeng, Y., Hao, D., Huete, A., Dechant, B., Berry, J., Chen, J., Joiner, J., Frankenberg, C., Bond-Lamberty, B., Ryu, Y., Xiao, J., Asrar, G., Chen, M., 2022. Optical vegetation indices for monitoring terrestrial ecosystems globally 17. https://doi.org/10.1038/s43017-022-00298-5

Zhang, C., Preece, C., Filella, I., Farré-Armengol, G., Peñuelas, J., 2017. Assessment of the Response of Photosynthetic Activity of Mediterranean Evergreen Oaks to Enhanced Drought Stress and Recovery by Using PRI and R690/R630. Forests 8, 386. https://doi.org/10.3390/f8100386

Zlobin, I.E., Kartashov, A.V., Pashkovskiy, P.P., Ivanov, Y.V., Kreslavski, V.D., Kuznetsov, V.V., 2019. Comparative photosynthetic responses of Norway spruce and Scots pine seedlings to prolonged water deficiency. J. Photochem. Photobiol. B 201, 111659. https://doi.org/10.1016/j.jphotobiol.2019.111659

7 APPENDICES

Appendix 1: Seedling material

Figure A1. *Pinus sylvestris* seedlings 6C, 30C, 25C, and 28C (above) assigned as control (C) plants before the start of the experiment. *Pinus sylvestris* seedlings 9D, 55D, 54D, and 10D (below) assigned as drought (D) plants before the start of the experiment.

Appendix 2. Material collection schedule

Table A1. Material collection schedule

DATE	DATE_ID	LL_R	PIGMENT	Fv/Fm	LWP	SM	HSI
8/9/2022	PD1	X	X	X	X	X	X
8/10/2022	PD2						
8/11/2022	PD3				X	X	
8/12/2022	PD4					X	X
8/13/2022	PD5						
8/14/2022	PD6						
8/15/2022	D1	X	X	X	X	X	X
8/16/2022	D2				X	X	X
8/17/2022	D3						
8/18/2022	D4			X	X	X	X
8/19/2022	D5			X	X	X	X
8/20/2022	D6						
8/21/2022	D7						
8/22/2022	D8			X	X	X	X
8/23/2022	D9			X	X	X	X
8/24/2022	D10			X	X	X	X
8/25/2022	D11			X	X	X	X
8/26/2022	D12						
8/27/2022	D13						
8/28/2022	D14						*
8/29/2022	D15			X	X	X	X
8/30/2022	D16			X	X	X	X
8/31/2022	D17	X	X	X	X	X	X
9/1/2022	D18						
9/2/2022	R1			X			X
9/3/2022	R2			X	X	X	X
9/4/2022	R3						
9/5/2022	R4			X	X		X
9/6/2022	R5						
9/7/2022	R6			X	X		X
9/8/2022	R7	X	X		X	X	X

PD=Pre-Drought, D=Drought, R=Recovery

*Diurnal measurements; images taken every 30 minutes from 8:30 to 17:30

Appendix 3. Images of set-up

Figure A2. Three open dark-adaptation clips on the primary shoot of a sample plant.

Figure A3. GFS3000 measuring head cuvette with needles inside (left) and the whole setup (right).

Appendix 4. Distance and angle to plant from HSI camera

Table A2. Distance and angle to the top of each plant shoot form HSI camera lens. Distance is in cm, and angle is an off-nadir angle.

Plant ID	Distance (cm)	Angle (°)
9D	102	8.9
6C	101	8.4
55D	102	19.7
30C	107	17.4
54D	97	18.9
25C	97	15.1
10D	101	19.2
28C	108	13.9

Appendix 5. Wavelengths of HSI spectral dimensions

Table A3. Wavelengths and corresponding bandwidths used of Aug 9th, and Aug 31st & Sep 8th as reported by HSI metadata. Wavelength corresponds to the position (nm) of the center of the signal, and FWHM bandwidth refers to the width of the signal at 50% of its maximum intensity.

	Aug 09		Aug 31 & Sep 08	
Band nr.	Wavelength (nm)	FWHM bandwidth (nm)	Wavelength (nm)	FWHM bandwidth (nm)
1	500	0	500	0
2	507.1	0	507.1	0
3	514.3	13	514.3	13
4	521.4	13	521.4	13
5	528.6	13	528.6	13
6	531	13	531	13
7	535.7	13	535.7	13
8	542.9	13	542.9	13
9	550	13	550	13
10	557.1	13	557.1	13
11	564.3	12	564.3	12
12	571.4	12	570	12
13	578.6	12	571.4	12
14	585.7	11	578.6	12
15	592.9	11	585.7	11
16	600	11	592.9	11
17	607.1	15	600	11
18	614.3	17	607.1	15
19	621.4	16	614.3	17
20	628.6	14	621.4	16
21	635.7	13	628.6	14
22	642.9	16	635.7	13
23	650	15	642.9	16
24	657.1	13	650	15
25	664.3	14	657.1	13
26	671.4	14	664.3	14
27	678.6	13	671.4	14
28	685.7	14	678.6	13
29	692.9	14	685.7	14
30	700	14	692.9	14
31	707.1	14	700	14
32	714.3	13	707.1	14
33	721.4	13	714.3	13
34	728.6	14	721.4	13
35	735.7	14	728.6	14
36	742.9	14	735.7	14
37	750	14	742.9	14
38	757.1	13	750	14
39	764.3	13	757.1	13
40	771.4	13	764.3	13
41	778.6	13	771.4	13
42	785.7	13	778.6	13
43	792.9	13	785.7	13
44	800	13	792.9	13
45	807.1	17	800	13
46	814.3	17	807.1	17
47	821.4	18	814.3	17
48	828.6	18	821.4	18
49	835.7	19	828.6	18
50	842.9	18	835.7	19
51	850	17	842.9	18
52	-	-	850	17

Appendix 6. Packages and R functions for HSI processing

Packages:

[[1]]
Wickham H (2016). _ggplot2: Elegant Graphics for Data Analysis_. Springer-Verlag New York. ISBN 978-3-319-24277-4, https://ggplot2.tidyverse.org.

[[2]]
Hijmans R (2023). _raster: Geographic Data Analysis and Modeling_. R package version 3.6-20, https://CRAN.R-project.org/package=raster.

[[3]]
Wickham H, Vaughan D, Girlich M (2023). _tidyr: Tidy Messy Data_. R package version 1.3.0, https://CRAN.R-project.org/package=tidyr.

[[4]]
Tuszynski J (2021). _caTools: Tools: Moving Window Statistics, GIF, Base64, ROC AUC, etc_. R package version 1.18.2, https://CRAN.R-project.org/package=caTools.

[[5]]
Wickham H (2007). "Reshaping Data with the reshape Package." _Journal of Statistical Software_, *21*(12), 1-20. http://www.jstatsoft.org/v21/i12/.

[[6]]
Pebesma E (2018). "Simple Features for R: Standardized Support for Spatial Vector Data." _The R Journal_, *10*(1), 439-446. doi:10.32614/RJ-2018-009 https://doi.org/10.32614/RJ-2018-009, https://doi.org/10.32614/RJ-2018-009.

Pebesma E, Bivand R (2023). _Spatial Data Science: With applications in R_. Chapman and Hall/CRC. https://r-spatial.org/book/.

```r
# Functions written for post-processing of HSI data for
# 2022 Master's thesis data by Iiro Miettinen

# Packages
library(ggplot2)
library(raster)
library(tidyr)
library(caTools)
library(reshape2)
library(sf)


# False RGB image with manual label input
RGB_image_fun <- function(img) {
  # blue band
  rst.blue <- raster(img[,,3])
  # green band
  rst.green <- raster(img[,,9])
  # red band
  rst.red <- raster(img[,,26])
  # plot false RGB image
  raster::plotRGB(x=stack(rst.blue, rst.green, rst.red), r=3, g=2, b=1,
                  scale=1, stretch="lin")

  # manual selection of lables points
  print("CLick 9 D")
  temp <- locator(1)
  text(temp, "9 D", col="white", cex=2.5)
  print("CLick 6 C")
  temp <- locator(1)
  text(temp, "6 C", col="white", cex=2.5)
  print("CLick 55 D")
  temp <- locator(1)
  text(temp, "55 D", col="white", cex=2.5)
  print("CLick 30 C")
  temp <- locator(1)
  text(temp, "30 C", col="white", cex=2.5)
  print("CLick 54 D")
  temp <- locator(1)
  text(temp, "54 D", col="white", cex=2.5)
  print("CLick 25 C")
  temp <- locator(1)
  text(temp, "25 C", col="white", cex=2.5)
  print("CLick 10 D")
  temp <- locator(1)
  text(temp, "10 D", col="white", cex=2.5)
  print("CLick 28 C")
  temp <- locator(1)
  text(temp, "28 C", col="white", cex=2.5)

  recordPlot(load = NULL, attach = NULL)

}
```

```r
# Function for calulcating the ratio of any two bands, used for PRI
band_ratio_fun <- function(img,band_1,band_2) {
  (img[,,band_1] - img[,,band_2]) / (img[,,band_1] + img[,,band_2])
}

# Function for calulcating red edge position (REP)
REP_fun <- function(img) {
  Ri <- (img[,,27]+img[,,42])/2 # 671.4 nm, 778.6 nm
  REP <- 700+40*((Ri - img[,,31]) / (img[,,37] - img[,,31])) # 700, 742.9 nm
}

# Function for calulcating MTCI
MTCI_fun <- function(img) {
  MTCI <- (img[,,38] - img[,,32]) / (img[,,32] - img[,,28]) # 754, 709, 681 nm
}


# Function for calulcating NDVI
NDVI_fun <- function(data) {

  # NIR band
  NIR <- data[,,52] # 850 nm

  # mean of red bands
  RED <- apply(data[,,c(23:27)],c(1,2), mean) # 640-670 nm

  # NDVI formula
  NDVI <- (NIR - RED) / (NIR + RED)
}



# Function for graphing a PRI image
PRI_graph_fun <- function(band) {
  # re-format band raster to a matrix
  band <- raster::as.matrix(band)

  # Re-format to long format
  spec_melt <- melt(band, varnames=c("x", "y"), value.name = "value")

  # Plot
  ggplot() +
    geom_raster(data = spec_melt, aes(x=x, y=y, fill=value)) +
    theme_void() +
    scale_fill_steps(limits=c(-0.03, 0.03), breaks=c(-0.03, -0.02, -0.01,
                                                     0, 0.01, 0.02, 0.03),
                     low="orange2", high="blue", na.value="transparent") +
    labs(fill=" ")

}


# Function for graphing a REP image
REP_graph_fun <- function(band) {
  # re-format band raster to a matrix
  band <- raster::as.matrix(band)

  # Re-format to long format
  spec_melt <- melt(band, varnames=c("x", "y"), value.name = "value")

```

```
  # plot
  ggplot() +
    geom_raster(bata = spec_melt, aes(x=x, y=y, fill=value)) +
    theme_void() +
    scale_fill_steps(limits=c(718, 725), breaks=c(718, 719, 720,
                                                  721, 722, 723,
                                                  724, 725),
                     low="orange2", high="blue", na.value="transparent") +
    labs(fill=" ")

}

# Function for graphing a MTCI image
MTCI_graph_fun <- function(band) {
  # re-format band raster to a matrix
  band <- raster::as.matrix(data)

  # Re-format to long format
  spec_melt <- melt(band, varnames=c("x", "y"), value.name = "value")

  # plot
  ggplot() +
    geom_raster(data=spec_melt, aes(x=x, y=y, fill=value)) +
    theme_void() +
    scale_fill_steps(limits=c(2, 8), breaks=c(2:8),
                     low="orange2", high="blue", na.value="transparent") +
    labs(fill=" ")

}

# Function to convert img to a NDVI filetered raster stack
array_to_stack <- function(img) {
  # mask based on NDVI values > 0.7
  NDVI <- NDVI_fun(img)
  NDVI[NDVI < 0.7] <- NA
  mask_raster <- raster(NDVI)

  # empty array to store masked raster layers
  stack_temp <- stack()

  # loop through all layers of img
  for (i in 1:dim(img)[3]) {
    layer_temp <- raster(img[, , i])
    raster_temp <- mask(layer_temp, mask_raster)
    stack_temp <- addLayer(stack_temp, my_raster)
  }

  stack_temp

}


# Function for calculating mean value (R or index) in a circle mask area
# input circle origin coordinates, radius and raster with NDVI filtering
band_mean_fun <- function(cx, cy, r, band) {
  # re-format band raster to a matrix
  df <- raster::as.matrix(band)
  # re-format to  long format
  df <- melt(df, varnames=c("x", "y"), value.name = "value")

```

```
  # calculate the area of the circle
  circle_area <- pi * r^2
  # calculate the distance from the center for each point
  df <- df %>% mutate(distance = sqrt((x - cx)^2 + (y - cy)^2))
  # subset the data frame to extract the points within the circle
  subset_df <- df %>% filter(distance <= r)

  # calculate the mean of the values within the circle
  mean_value <- mean(subset_df$value, na.rm=T)

}


# Function for 100 random pixel spectral graphs and average
# input filtered raster stack
pixel_spec_fun <- function(cx, cy, r, img, title) {
  # Re-format to long format with coordinates x, y, and z
  df <- melt(img, varnames=c("x", "y", "z"), value.name = "value")

  # calculate the area of the circle
  circle_area <- pi * r^2
  # calculate the distance from the center for each point
  df <- df %>% mutate(distance = sqrt((x - cx)^2 + (y - cy)^2))
  # subset the data frame to extract the points within the circle
  subset_df <- df %>% filter(distance <= r)

  #
  subset_df$pixel_id <- as.character(paste(subset_df$x, subset_df$y,
                                           sep=" / "))
  # list of all pixels with unique identifiers in the maksed area
  pixel_id_list <- unique(subset_df$pixel_id)
  # sample 100 random pixels from list of unique identifiers
  subset_df <-  subset(subset_df, subset_df$pixel_id
                       %in% sample(pixel_id_list, 100))

  # make new wavelength column based on band number
  wavelengths <- c(c(500.000000,507.100000,514.300000,521.400000,528.600000,
                     531.000000,535.700000,542.900000,550.000000,557.100000,
                     564.300000,570.000000,571.400000,578.600000,585.700000,
                     592.900000,600.000000,607.100000,614.300000,621.400000,
                     628.600000,635.700000,642.900000,650.000000,657.100000,
                     664.300000,671.400000,678.600000,685.700000,692.900000,
                     700.000000,707.100000,714.300000,721.400000,728.600000,
                     742.900000,750.000000,757.100000,764.300000,771.400000,
                     778.600000,785.700000,792.900000,800.000000,807.100000,
                     814.300000,821.400000,828.600000,835.700000,842.900000,
                     850.000000)

  for (i in c(1:length(wavelengths))) {
    subset_df[subset_df == i] <- wavelengths[i]
  }

  # remove NA-values
  subset_df <- na.omit(subset)

  # plot
  ggplot(subset_df) +
    # plot all 100 reflectance curves
    geom_line(aes(x=z, y=value, group=pixel_id), alpha=1/10) +
```

```
240     # plot mean of 100 curves
241     stat_summary(aes(x=z, y=value), fun=mean, geom="line",
242                  colour="red", linewidth=1) +
243     theme_bw() +
244     labs(x="wavelength (nm)", y= "Reflectance", title = title) +
245     # vertical lines to demonstrate bands used for PRI at 531 and 570 nm
246     geom_vline(aes(xintercept=531),linetype=2,na.rm = T)+
247     geom_vline(aes(xintercept=570),linetype=2,na.rm = T)+
248     # coordinates optimized for PRI
249     coord_cartesian(ylim=c(0, 0.15), xlim=c(520, 600)) +
250     theme(legend.position = "none")
251 }
252
```

Appendix 7. Relative soil moisture timeseries

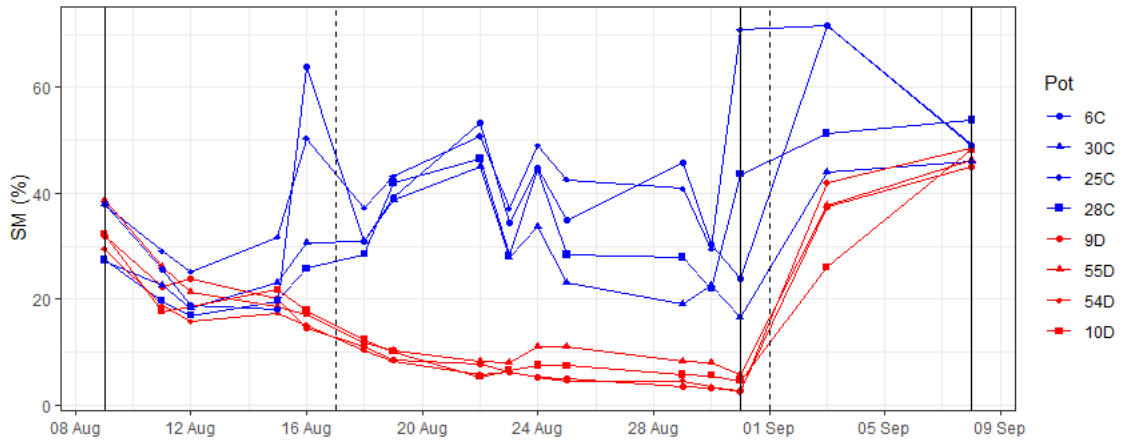

Figure A4. Timeseries relative soil moisture for the duration of the experiment. Control plants are denoted in blue and treatment plants in red. The black vertical lines denote the pre-drought (Aug 9th), height of drought (Aug 31st), and recovery (Sep 8th) dates. The vertical dotted lines denote the start of drought treatment (Aug 17th) and recommission of irrigation (Sep 1st).

Appendix 8. Leaf-level reflectance

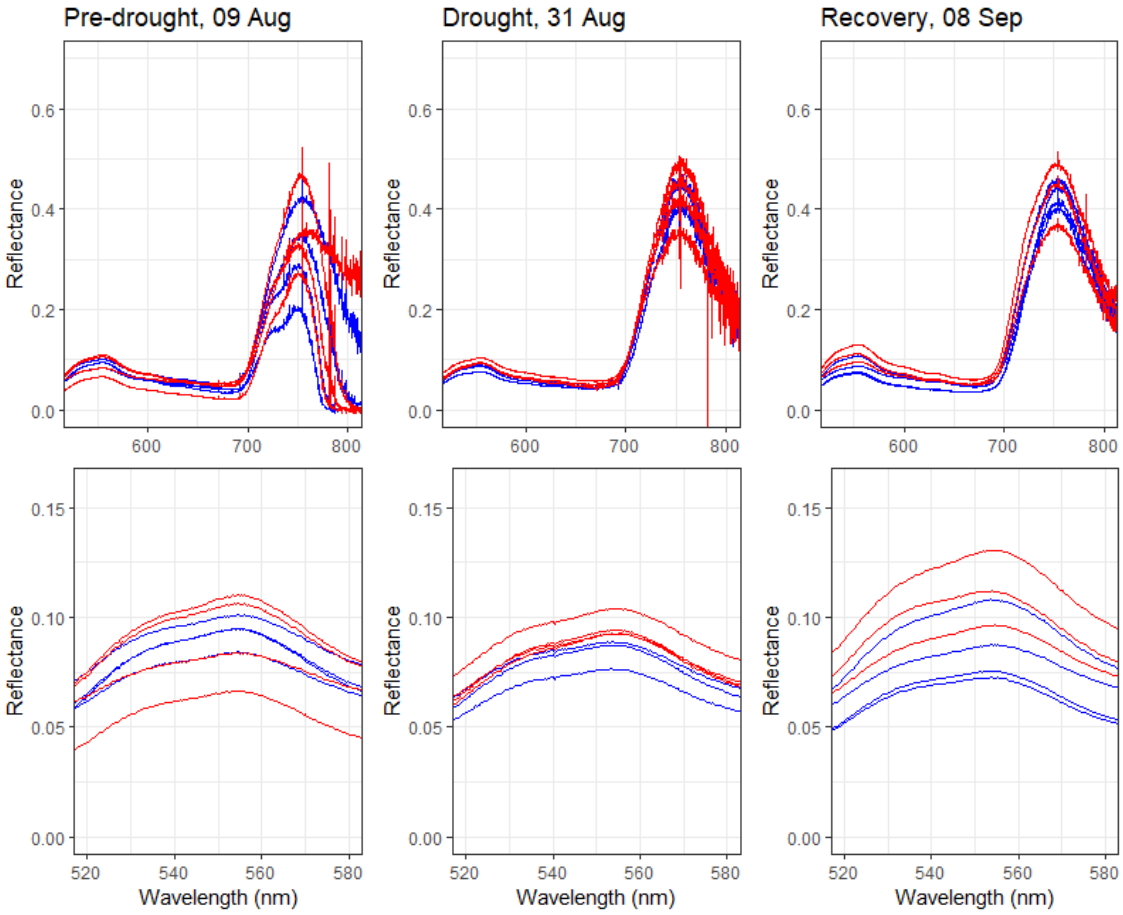

Figure A5. Reflectance curve in range 520-800 nm (above) and in range 520-580 nm (below) gained from non-imaging-based leaf level spectroscopy from three sampling days. Control plants are denoted in blue, and drought plants in red. Measurements were performed under a white LED light, which is why bands in the NIR (> 750 nm) are noisy and were not used to calculate indices in this thesis.

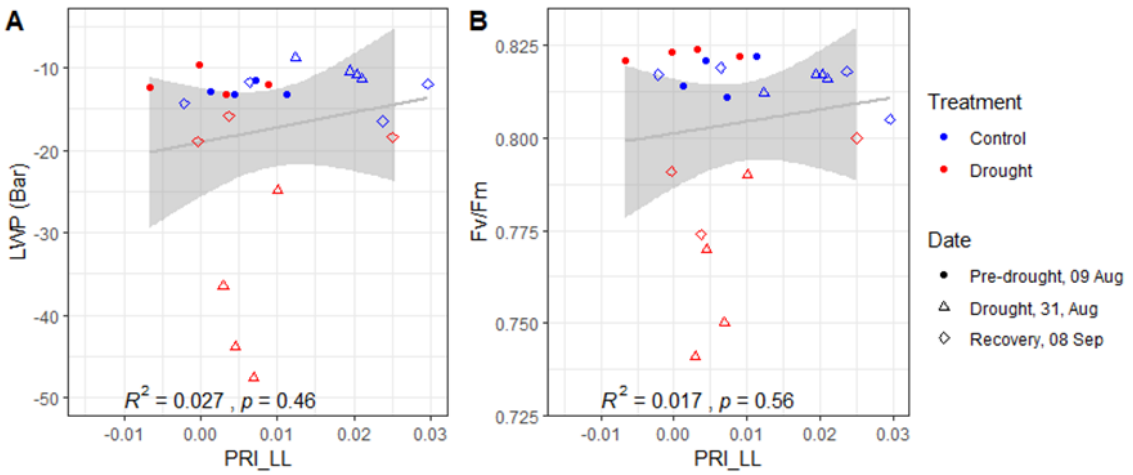

Figure A6. Relationship between A) leaf level PRI and LWP, B) leaf level PRI and F_v/F_m.

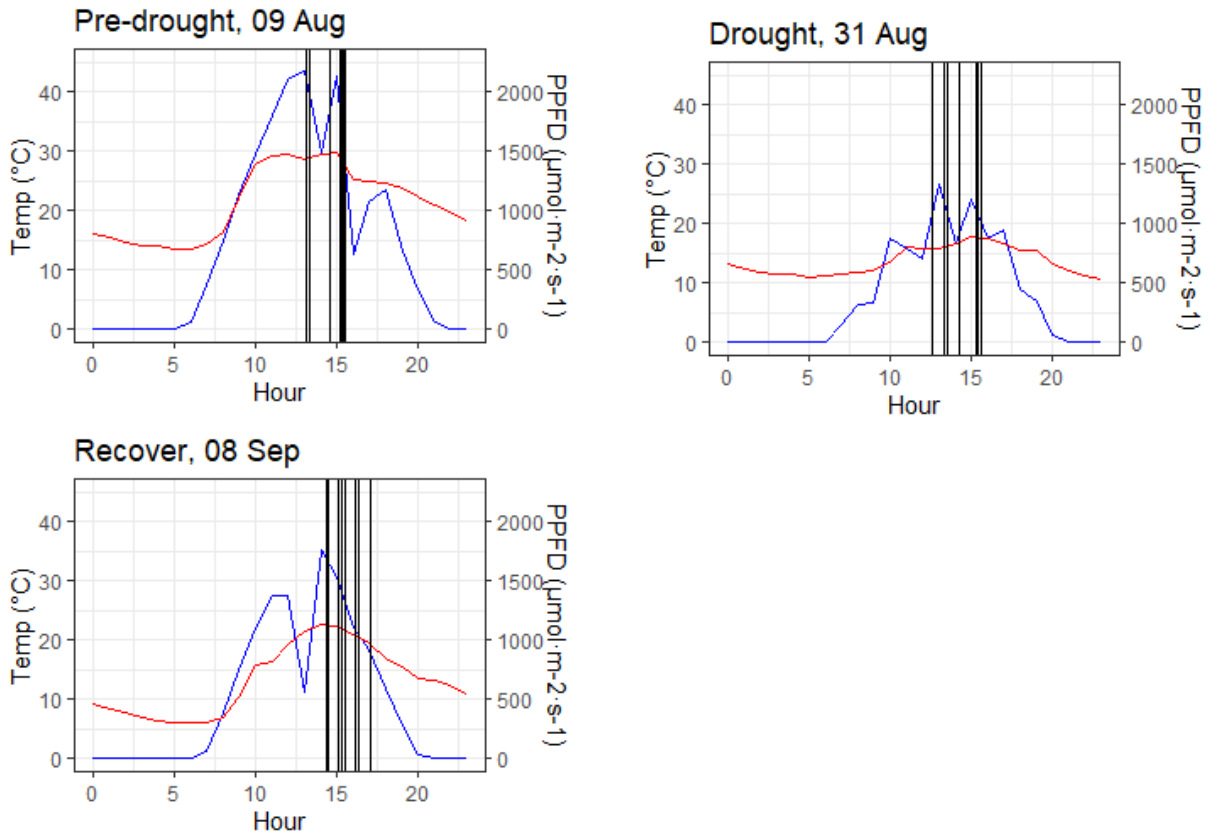

Figure A7. Timeseries of temperature (°C) in red and outdoor PPFD (µmol·m^{-2}·s^{-1}) in blue on three sampling days. The black vertical lines denote the time of leaf level reflectance measurements.

Appendix 9. HSI spectra

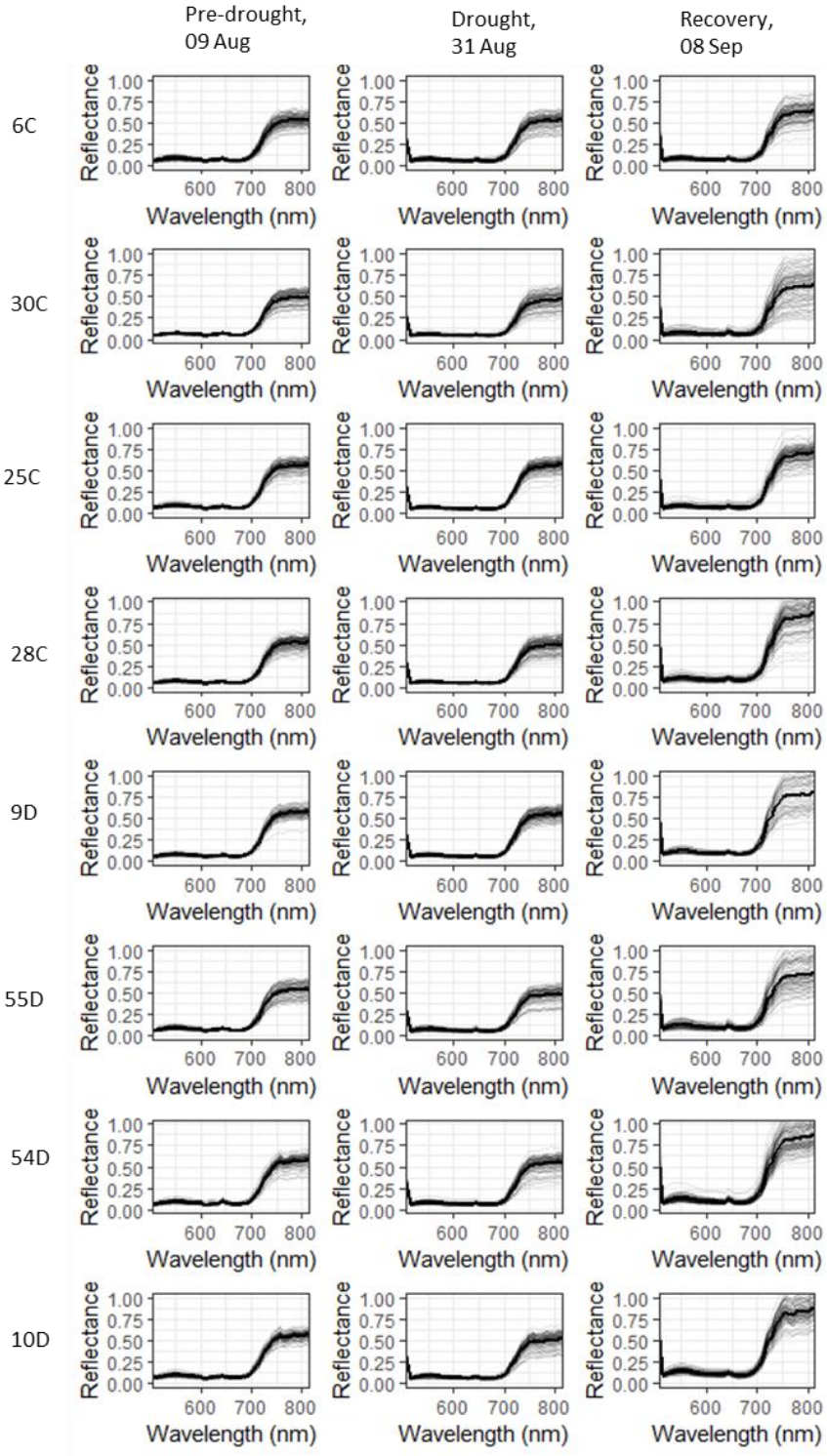

Figure A8. Reflectance spectra on 100 randomly sampled pixels (gray) and their average spectrum curve (black) for each sample plant on the three primary measuring days.

Appendix 10. Scatterplot matrix

Figure A9. Scatterplot matrix of VIs, and supporting and physiological variables. HSI_temp. is temperature (°C) at the time of HSI, LL_temp. at the time of leaf level spectroscopy. HSI_PPFD is PPFD (μmol·m^{-2}·s^{-1}) at the time of HSI, LL_PPFD at the time of leaf level spectroscopy. SM is relative soil moisture (%), LWP is leaf water potential (Bar), FvFm is maximum quantum yield of PSII photochemistry, MTCI is the MERIS terrestrial chlorophyll Index, REP is red edge position (nm), HSI_PRI is PRI from hyperspectral data, and LL_PRI is PRI from non-imaging-based leaf level reflectance.